Iceland Liechtenstein Norway grants
"Working together for a green, competitive and inclusive Europe"

GREENCAM for tomorrow

UNIVERSITY OF BUCHAREST

NTNU
Norwegian University of Science and Technology

UNIVERSITY OF BUCHAREST
VIRTUTE ET SAPIENTIA

FACULTY OF CHEMISTRY

MSc. Thesis

Master student: GUZO NICOLAE-CRISTIAN

Thesis Advisor:

Prof. SIMONA MARGARETA COMAN, PhD

2021

Disclaimer: This was realised with the EEA Financial Mechanism 2014-2021 financial support. Its content (text, photos, videos) does not reflect the official opinion of the Programme Operator, the National Contact Point and the Financial Mechanism Office. Responsibility for the information and views expressed therein lies entirely with the author(s).

UNIVERSITY OF BUCHAREST
VIRTUTE ET SAPIENTIA

FACULTY OF CHEMISTRY

DEPARTAMENT OF ORGANIC CHEMISTRY, BIOCHEMISTRY AND CATALYSIS

MSc. Thesis

From humin wastes to Carbon Quantum Dots (CQDs) photocatalytic nanocomposites

Master: Chemistry of Advanced Materials

Master student: GUZO NICOLAE-CRISTIAN

Thesis Advisor:

Prof. SIMONA MARGARETA COMAN, PhD

June – July, 2021

CONTENT

INTRODUCTION

Last decades confirmed catalysis as a strategic field of science representing the new way to meet the challenges of sustainability. In this context, one of the big challenges is the development of cleaner catalytic processes to convert biomass to multiple platform molecules as strategic precursors for valuable products. At the same time, the production of chemicals should be made in an economical, ethical and environmentally friendly way and this requires complete and efficient valorization of non-edible feedstock. As an example, during the acid-catalyzed dehydration of carbohydrates for the production of renewable bulk chemicals large amounts of so-called humins, which are carbonaceous, insoluble by-products, are typically formed. The commercial processes for the acid-catalyzed conversion are, therefore, seriously hampered by the extensive formation of humins by-products that leads to great losses of the feed (around 10-50% carbon loss) and, in this way, to great efficiency losses in biorefinery operations. In order to improve the efficiency of acid-catalyzed conversions of sugars and, in this way, to improve the economically value of the process, humins should be recovered and valorized.

Photocatalysis is based on the use of photons to drive chemical reactions, thus enabling to obtain several benefits simultaneously, such as: (1) the reactions can be carried out at lower temperatures; (2) toxic substances can be easily degraded; (3) processes can be achieved in a sustainable and environmentally friendly way. Among different UV-active materials titanium dioxide (TiO_2) is the benchmark photocatalyst, due to its strong oxidizing capacity, long-term photostability, commercial availability and low cost. However, the large band gap (3.20 eV) makes TiO_2 inactive under visible light irradiation which largely restricts its practical applications. Therefore, the development of visible light active photocatalysts and techniques to shift the range of light absorption of UV active compounds towards the visible light range has gained increasing importance in the photocatalytic research. In view of their attractive optical properties and up-conversion in particular, a nanocomposite of carbon quantum dots (CQDs) and TiO_2 is expected to realize the efficient usage of the full spectrum of sunlight. However, even though the combination of CQDs with metal oxides can give a significant increase in the photocatalytic activity comparing to the metal-oxides alone, there is still a lot of work to be done in order to increase the lifespan of the as prepared catalysts and maintain their catalytic activity throughout the time.

1. LITERATURE SURVEY

1.1 Biomass and its composition

Biomass (i.e., any renewable organic matter including agricultural food and feed crop residues, energy crops and trees, wood and wood residues, aquatic plants and animal wastes) is a very valuable feedstock, both for the production of chemicals and of novel fuels, which in the future could replace crude oil and gas as the current major raw materials [1]. For such processes a controlled de-functionalization is necessary rather than the functionalization used in the chemical industry. Unfortunately, this means that most of the developed processes in petrochemical and chemical industry are not suitable for converting biomass and alternative pathways for the production of fuels and chemicals should be developed. Moreover, from sustainable development and environment protection reasons, an efficient biorefinery unit should provide a complete valorization of the biomass source by performing the overall processes with a minimum loss of energy and mass and should maximize the overall value of the production chain with the minimum formation of wastes. For the efficient utilization of biomass, it will be crucial to create a similar comprehensive network of process chains.

Lignocellulose is the most abundant biomass feedstock, with an annual growth of 170 billion tons and it does not directly compete with food supplies because of its non-edible nature. [2] Lignocellulose is mainly composed of three biopolymers: cellulose (28–50%, polymer of glucose), hemicellulose (20–35%, polymer of C5 and C6 carbohydrates), and lignin (15–28%, aromatic polymer), along with smaller amounts of pectin (generic term for a polymer comprising galacturonic acid units of at least 65%), protein, extractives (triglycerides, terpenes, pigments, waxes, etc.) and ash (Figure 1).

From the chemically point of view, ***cellulose*** is a non-branched long chain water-insoluble polysaccharide consisting of several hundred up to tens of thousands of D-glucose units linked to each other by β-(1,4)-glycosidic bonds. These long-chain cellulose polymers are linked together by physical (i.e., hydrogen and van der Waals) bonds, which cause the cellulose to be packed into microfibrils [3].Unlike cellulose, ***hemicellulose*** has easily hydrolysable branches with short lateral chains consisting of C6-sugars (glucose, mannose and galactose), C5-sugars (mainly arabinose and xylose) and uronic acids (e.g., 4-*o*-methylglucuronic, D-glucuronic, and D-galactouronic acids), linked each other by β-(1,4)-glycosidic bonds (predominantly) and by α-(1,3)-glycosidic bonds (occasionally) [3]. The

fourth component, which is present in a quite considerable amount and it is called ***lignin***. Lignin is acting as glue, holding together the cellulose microfibrils and hemicellulose fibers, imparting structural support, impermeability, and resistance against microbial attack. It comprises 15–28% of lignocellulosic biomass and is the only scalable renewable resource, consisting of abundant aromatic chemicals derived from p-coumaryl, coniferyl, and sinapyl alcohols. [3]

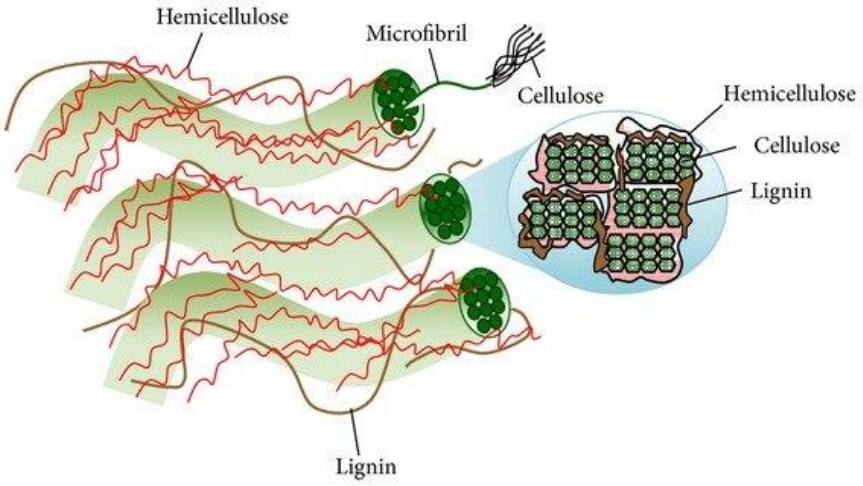

Figure 1. Composition of lignocellulose [3]

Hence, the efficient fractionation of lignocellulose into separated streams of these three polymers is often the entry point for a fruitful bio-refinery as it opens the possibility of subsequent transformations to high-value chemicals and fuels. In this context, reductive catalytic fractionation (RCF) of lignocellulose has received tremendous attention, providing stable lignin oil containing high-value phenolic mono-, di- and oligomers as well as a vaporizable solid carbohydrate pulp that can be used for the production of paper, fine chemicals, or biofuels. [4]

1.2 The biorefinery and biomass valorization

Due to the increasing pressure on the industries to step back from the fossil fuel based processes, they needed a green alternative. What is required is a source of carbon analogous to petrol, where a complex mixture of chemicals can be converted in several high-value molecules, through the development of efficient refinement procedure including cracking, chemical modification and separation in the so-called ***bio-refineries*** defined as “a facility or a

network of facilities that converts biomass including waste into a variety of chemicals, biomaterials and energy, maximizing the value of the biomass and minimizing waste" (National Renewable Energy Laboratory (NREL)). Advanced biorefineries are analogous in many ways to today's petrorefineries [5]. A comparison between these 2 types of refineries is presented in the Figure 2:

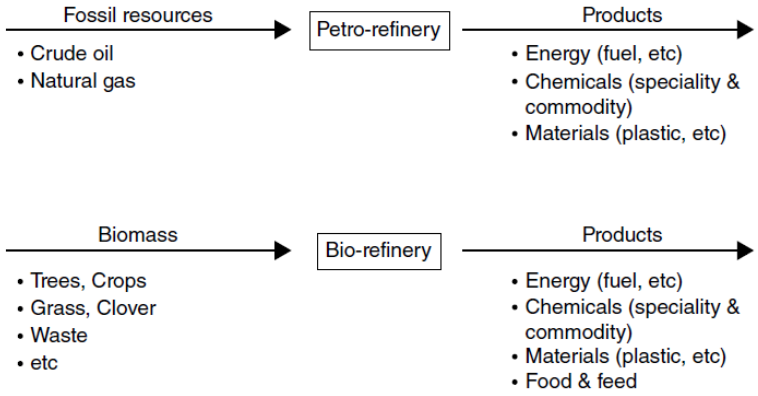

Figure 2. Comparison between petrorefinery and biorefinery [5]

Similarly to oil-based refineries, where many energy and chemical products are produced from crude oil, biorefineries produce many different industrial products from biomass. These include low-value high-volume products such as transportation fuels (e.g. biodiesel, bioethanol), commodity chemicals and materials and high-value low-volume products or specialty chemicals such as cosmetics or nutraceuticals (i.e., food containing health - giving additives and having medicinal benefit).

The obvious alternative to fossils is biological material (biomass) from living or recently living organisms, not metabolized for thousands of years into petrol and coal, thus not concurring to CO_2 emissions. In principle, the biorefining concept has similar objectives as today's petroleum refineries, but the feedstocks are totally different. In chemical and pharmaceutical industry are required molecules that serve as a source of carbon atoms. This is necessary in order to be able to shape the compounds already existent, into the ones are needed. Driven by this, multiple paths in order to provide the industry with the necessary materials and molecules were taken, but the one more interested is the biomass valorization.

From other perspective, people realized that it is no easy job not only in finding renewable sources of carbon for the chemical and pharmaceutical industries but also in getting rid of the wastes generated by different industries. On one hand, the chemical industry does not produce that much of carbon dioxide, but on the other hand, these industrial processes produce a lot of other wastes, and in order to get rid of them, we have to use many different

procedures that sometimes can be even more expensive than the production process itself. This fact, has led to an interest in other ways of getting rid of the wastes created by mankind, and one of the most promising ones is the waste valorization. This procedure implies transforming by-products of industrial processes into compounds that can serve as raw materials or starting points for other transformations based on the molecules that we obtain.

1.3 Platform molecules and added-value products

A prime objective in the catalytic conversion of lignocellulosic feedstocks is the improving of the catalyst's efficiency and selectivity towards value-added products. However, the incorporation of compatible catalytic processes in the actual infrastructure of petrochemical industry plants requires as biomass feedstocks to be converted to building block chemicals with fewer oxygenated groups. These building block chemicals (also known as "platform molecules") are molecules with multiple functional groups that possess the potential to be transformed into new families of useful chemicals. The most important 15 platform molecules that can be produced from sugars via biological or chemical conversions and can be subsequently converted to a number of high-value bio-based chemicals or materials are given in Table 1.

Table 1. Building blocks obtained from biomass [6]

Building Blocks
1,4 succinic, fumaric and malic acids
2,5 furan dicarboxylic acid
3 hydroxy propionic acid
aspartic acid
glucaric acid
glutamic acid
itaconic acid
levulinic acid
3-hydroxybutyrolactone
glycerol
sorbitol
xylitol/arabinitol

Some of building blocks were the subject of intense research and development during the past few years (such as 5-hydroxymethylfurfural, furfural, levulinic, lactic and succinic acids, as

well as new industrial derivatives from sorbitol) while there was a comparatively modest interest for organic acids (such as aspartic, malic, fumaric, glutamic and itaconic acids).

1.4 Humins: structure and applications

The synthesis of 5-hydroxymethylfurfural (HMF), 5-alkoxymethylfurfural and levulinic acid (LA) by acid catalyzed fructose dehydration, is complemented with the formation of substantial quantities of a black tarry by-product, a complex polyfuranic polymer, called humins [7]. Humins are heterogeneous amorphous biomacromolecules, considered to have the idealized morphology of spherical core-shell architecture [8]. The chemical structure of humins consists of furfural and hydroxymethylfurfural moieties also with carbohydrate, levulinate and alkoxymethylfurfural chains linked together into macromolecules by ether, acetal bonds or aliphatic linkages. The nature of terminal groups could be of carboxylic, ketone, aldehyde and/or hydroxyl nature. Also, the presence of certain solvents such as acids or alcohols during the carbohydrate dehydration reactions could lead to the appearance of other functional groups such as alkoxy and ester groups [9].

The mechanism of the humins formation is supposed to be an acid catalyzed condensation between its formed intermediates but it is also possibly to be formed directly from the starting carbohydrate during their transformation to HMF/MMF/LA, leading to a network of furan rings [10] (Figure 3). The yield of humins is influenced by process parameters such as the type of substrate, time, temperature, and type of acid catalyst. For example, in the case of cellulose conversion to LA, humins yields range from 25–45 wt.%. In the case of HMF production, 10–50 wt. % of sugar substrates are converted into humins. Humins are thus a major waste fraction during sugar conversion [11]. However, despite intensive investigation on the various conversion routes of polysaccharides, understanding of the pathway of humins formation is poor. Furthermore, a clear description of the nature of humins itself is lacking. Generally, humins consists of carbon-rich agglomerate particles. It is composed of approximately 50–66 wt. % C, 25–46% wt.% O, and the remainder is H. [11]

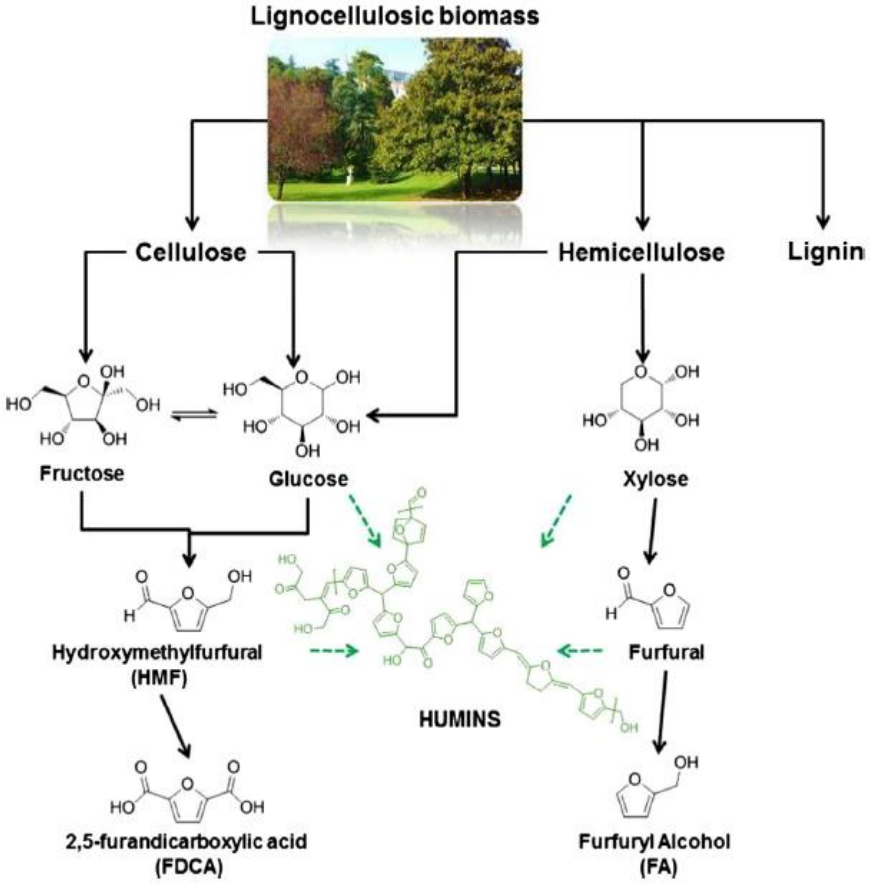

Figure 3. Mechanism of formation of humins [7]

Efforts have been made to suppress the formation of humins, for example, by co-feeding alcohol to stabilize HMF by esterification and thus prevent its further conversion to humins. However, the yield of humins is still 14–22 wt. %. Its main application is still limited to energy and heat applications such as burning and gasification but its valorization into higher added-value applications will be the key for making biomass conversion processes economically feasible. [7]

1.5 Carbon Quantum Dots (CQDs)

Quantum dots are particles of size smaller than Bohr exciton radius (≤10 nm), usually made from semi-conductors. Carbon-based quantum dots consisting of graphene quantum dots (QGDs) and carbon quantum dots (CQDs, C-dots or CDs) are a new class of carbon nanomaterials with sizes below 10 nm. They were first obtained during the purification of single-walled carbon nanotubes through preparative electrophoresis in 2004 [12] and then via laser ablation of graphite powder and cement in 2006 [13]. While carbon is a black material, with a low solubility in water and weak fluorescence, carbon-based quantum dots possess a

good solubility and strong luminescence, for which they are referred to as carbon nanolights [14].

Moreover, compared to traditional semiconductor quantum dots and organic dyes, photo luminescent carbon-based quantum dots are superior in terms of high (aqueous) solubility, robust chemical inertness, facile modification and high resistance to photo bleaching. On one hand the superior biological properties of carbon-based quantum dots, such as low toxicity and good biocompatibility, entrust them with potential applications in bioimaging, biosensor and drug delivery. On the other hand, the outstanding electronic properties of carbon-based quantum dots as electron donors and acceptors, causing chemiluminescence and electrochemical luminescence, endow them with wide potentials in optronics, catalysis and sensors. [15]

Since their discovery, Carbon Quantum Dots (Carbon QDs or CQDs) were heavily studied in order to find the optimal method for their synthesis and viable methods for their functionalization. Roughly, the methods of synthesis can be divided in two main groups – the first one being the so called "bottom-up" and the other one being "top-down" [16]. Using both of the methods, the nano-particles that are obtained can be modified either during the synthesis itself or after the synthesis is done.

Table 2. Methods of synthesis for Carbon QDs with their advantages and disadvantages. [16]

	Methods	Merits	Demerits
Top-down	Laser ablation	Controllable morphology and size	Complicated operation, high cost
	Electrochemical oxidation	High purity, high yield, controllable size, good reproducibility	Complicated operation
	Chemical oxidation	Easy operation, large scale production, no elaborate equipment	Non-uniform size distribution
	Ultrasonic treatment	Easy operation	Instrumental wastage, high energy cost
Bottom-up	Microwave synthesis	Short reaction time, uniform size distribution, easy size control	High energy cost
	Thermal decomposition	Easy operation, solvent-free, low cost, large scale production	Non-uniform size distribution
	Hydrothermal treatment	High quantum efficiency, low cost, non-toxicity	Low yield

Nevertheless, there are also some issues that need to be considered prior the synthesis: (I) carbonaceous aggregation during carbonization, which can be avoided by using electro-chemical synthesis, confined pyrolysis or solution chemistry methods, (II) size control and uniformity, which is important for uniform properties and mechanistic study, and can be optimized via post-treatment, such as gel electrophoresis, centrifugation, and dialysis and (III) surface properties that are critical for solubility and selected applications, which can be tuned

during preparation or post-treatment. [15] In the Table 2 there are summarized the advantages and disadvantages of several methods for obtaining Carbon QDs.

As in the cases of many other new materials to the world, CQDs are heavily studied in order to figure out all the suitable applications for them. This part of their research is very important due to the fact that without important application, CQDs will remain just a demonstration of skill in the synthesis of advanced materials.

The most interesting application for us is the photocatalysis. The interest in photo catalysis has been motivated in part by the realization that sunlight is effectively an inexhaustible energy source. However, the high energy of UV and short wavelength visible light may adversely damage organic compounds. The demonstrated capability of harnessing long wavelength light and energy exchange with solution species of CQDs offers an excellent opportunity for their use as photocatalysts in organic synthesis. Indeed, a recent study has indicated that smaller CQDs (1–4 nm) are effective NIR light-driven photocatalysts for selective oxidation of benzyl alcohol to benzaldehydes with good conversion efficiency (92%) and selectivity (100%), due to their excellent catalytic activity for H_2O_2 decomposition and NIR light driven electron transfer property [17]. Further studies suggested that the photo catalytic activity of CQDs can be effectively modulated by doping and by tailoring the surface groups. On the other hand, larger CQDs (5–10 nm) synthesized by electro-chemical ablation of graphite showed light-induced proton properties in solution, which can be used as acid catalysts to catalyze a series of organic transformations in aqueous media under visible light. [18]

1.6 TiO_2 and photocatalysis

Photocatalytic reactions driven by sunlight represent a promising way to address the increasing environmental and energy concerns. Therefore, developing and optimizing highly efficient photocatalysts under visible light has attracted worldwide attention.

To date, various photocatalytic semiconductors were used, but undoubted, titanium dioxide (TiO_2) is one of the most widely studied photocatalysts due to its abundance, low cost, low toxicity, superior photostability, and high intrinsic catalytic activity under UV illumination [18]. Among different TiO_2 powders, as called TiO_2 P-25 Degussa, with a relatively large surface area and an anatase to rutile phases ratio of about 3 to 1 is the standard material for photocatalytic reactions. However, in spite of all these advantages, the poor

responses to visible light caused by its wide band gap (3.0–3.2 eV), and the fast recombination of photogenerated electron-hole pairs had significantly hindered the application of TiO_2 in photocatalysis [19].

The photocatalytic properties of TiO_2 depend on its intrinsic properties, such as specific surface area, crystal phase and crystallinity [20]. Generally, large surface area resulted from porous structure is favorable to improve photocatalytic activity, as demonstrated for mesoporous TiO_2 [21]. However, large surface areas, which often result not only from porous structure but also from small particle size, usually correspond to the low anatase phase crystallinity. Unfortunately, the high degree of defects in this phase further promotes the recombination of photogenerated electrons and holes [22]. Thus, a preferred way to enhance the photocatalytic activity is the synthesis of TiO_2 materials with simultaneously increased anatase crystallinity and large surface area. Examples of such materials were reported in literature and two of them refer to nanocrystalline TiO_2 photocatalysts synthesized by co-modifying TiO_2 with ammonia and cetyltrimethylammonium bromide [22] or by modifying it with mesoporous SiO_2 [23]. Several other modifications have been made, such as carbon modified TiO_2 [24] and hydrothermal treatment at 400 ^{0}C in air [25].

In particular, modification of TiO_2 with carbon nanomaterials, such as carbon nanotubes, fullerenes and graphene, have been used to produce TiO_2/carbon composites with promising photocatalytic activities in the visible region [26]. However, both carbon nanotubes and graphene aggregate easily and are difficult to disperse in conventional solvents, which limit their applications [27]. In connection with this, recently have been shown that the conjugated structure of CQDs leads to the excellent electron transfer/reservoir properties, which is the key factor in enhancing the semiconductors photocatalytic activity [28].

CQDs have the great advantage of having a band gap that can be adjusted by simply changing the size of the nanoparticles. This allows them to easily absorb radiation from different areas of the solar spectrum. Therefore, by introducing CQDs as electron transfer/reservoir materials on the surface of TiO_2, the recombination rates of photogenerated carriers can be modified, allowing the improvement of photocatalytic performance and increasing photocatalytic activity in visible light. In this way, CQD@TiO_2 nanocomposites possess much improved photocatalytic activity, as Gray and co-workers [29] demonstrated. In addition, problems induced by carbon and graphene nanotubes are avoided.

OBJECTIVES

The main scope of the dissertation thesis was to extend the potential of humins valorization to the synthesis of CQDs. To reach this scope worthless humins by-product, generated in the glucose acid-dehydration, has been subjected to an environmentally friendly low-temperature hydrothermal process. The synthesized CQDs with optimized size, brightest blue fluorescence and highest QYs were then used as sensitizers in producing CQD@TiO_2 heterostructured nanocomposites. The photocatalytic activity of the as prepared CQDs@TiO_2 samples was evaluated in methylene blue (MB) dye degradation under the visible light irradiation.

2. Experimental Section

2.1 CQDs preparation

2.1.1 Humins synthesis

Since the glucose conversion is one of the most studied routes for making HMF, due to its commercial significance, in this study humins obtained from glucose dehydration were chose for the CQDs design. Humins were prepared in agree with a recently reported hydrothermal methodology applied in our laboratory [30] as follow: an aqueous solution containing D-glucose (36.0 g D-glucose in 200 ml water, 1.0M) and H_2SO_4 (1.078 g, 5.5 mM) were added into an autoclave and heated at 180 ^{0}C, for 7 h. Obtained humins were isolated by filtration, washed with water (300 mL), dried for 12 h at 80 ^{0}C, grounded and purified by Soxhlet extraction (Scheme 1).

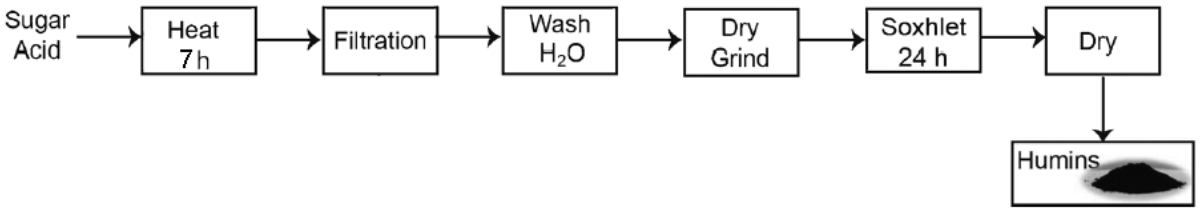

Scheme 1. Preparation and purification of humins

2.1.2 CQDs synthesis by hydrothermal treatment

CQDs were synthesized by applying the following hydrothermal treatment methodology: 20 mg of humins were dispersed in 20 mL of water in an autoclave. To this suspension 0.1 mL of glacial CH_3COOH was added and the obtained mixture was vigorously stirred at temperatures of 160-200 ^{0}C, for 4-12 h. After reaction, the obtained mixture was centrifuged at 8000 rpm for 40 min and the liquid phase was filtered through a Stericup Durapore filter with the pores of 0.22 μm on a polyvinylidene difluoride (PVDF) membrane. The obtained CQDs were denoted: $CQD_{T\text{-}h}$, where T – represent the synthesis temperature and h - represent the synthesis time.

For the $CQD_{180\text{-}12S}$ synthesis a separation protocol similar to that described in [31] was applied, as following: the obtained brown solution after the hydrothermal treatment of humins at 180^{0}C and 12 h was washed with dichloromethane to remove the adsorbed organic moieties (i.e., acetic acid and other small organic moieties from humins) and the aqueous solution phase was centrifuged at 8000 rpm for 40 min, filtered through a Stericup Durapore filter and concentrated under vacuum at 80 ^{0}C for 2 h.

2.2 CQDs@TiO_2 nanocomposites synthesis

For the synthesis of CQDs@TiO_2 nanocomposites, two kinds of TiO_2 materials were used: a commercial TiO_2 P-25 Degussa powder (consisting of ca. 85% anatase and 15% rutile in crystalline phase) and a modified TiO_2 synthesized from P25 powder by its treatment with NaOH. The two samples are denoted P-TiO_2 and M-TiO_2.

For the synthesis of M-TiO_2 sample 0.3 g P-TiO_2 powder was added to an aqueous solution of 30 mL NaOH (10 mol/L) and stirring for 1 h, at room temperature. Then, the mixture was slowly added into 40 ml autoclave and heated at 120 ^{0}C for 24 h under stirring. After cooling to the room temperature, the aqueous solution was separated by centrifugation and the sediment was washed with HCl solution (1 mol/L) until pH = 1, and subsequently washed with distilled water until pH = 7. After drying for 4 h, the sample was calcined for 2 h, at 450 ^{0}C.

CQDs@TiO_2 composites were obtained by a hydrothermal method, following a reported methodology by Zhang and co-workers [32]. Typically, 20 mL distilled water and 6 mL ethanol were mixed together, and then 0.4 g TiO_2 (P-TiO_2 or M-TiO_2) powder and 2 mL of aqueous solution of CQDs ($CQD_{180\text{-}4}$, $CQD_{200\text{-}4}$, $CQD_{180\text{-}12}$, $CQD_{180\text{-}12S}$) was added. The mixture was kept stirring for 4 h at room temperature to obtain a homogeneous suspension.

After that, the suspension was transferred into an autoclave with glass inner and maintained at 140 ^{0}C for 4 h. Resulted CQDs@TiO_2 composites were washed three times with water and collected by centrifugation at 6100 rpm, for 15 minutes. Finally, the separated solid was dried under vacuum at 60 ^{0}C for 6 h.

Eight samples were obtained and denoted as $CQD_{180\text{-}4}$@P-TiO_2, $CQD_{200\text{-}4}$@P-TiO_2, $CQD_{180\text{-}12}$@P-TiO_2, $CQD_{180\text{-}12S}$@P-TiO_2, $CQD_{180\text{-}4}$@M-TiO_2, $CQD_{200\text{-}4}$@M-TiO_2, $CQD_{180\text{-}12}$@M-TiO_2 and $CQD_{180\text{-}12S}$@M-TiO_2, where the subscript numbers represent the hydrothermal parameters, i.e., temperature and time, respectively, used for the CQDs synthesis from humins.

2.3 Characterization techniques

The prepared CQDs and CQD@TiO_2 materials were exhaustively characterized by techniques as: X-ray diffraction (XRD), ATR- and DRIFT-IR spectroscopy, UV-Vis spectroscopy, photoluminescence spectroscopy (PL), adsorption-desorption isotherms of liquid nitrogen at 77K, elemental analysis, thermogravimetric-differential thermal analysis (TG-DTA), transmission electron microscopy (TEM) and energy dispersive X-ray spectroscopy in scanning transmission electron microscopy (STEM-EDS). .

Powder X-ray Diffraction patterns were collected at room temperature using a Shimadzu XRD-7000 apparatus with the Cu Kα monochromatic radiation of 1.5406 Å, 40 kV, 40 mA at a scanning rate of 0.1 2θ min^{-1}, in the 2θ range of 5^0–80^0.

ATR-FTIR spectra were recorded and collected by a Bruker Tensor-II FTIR spectrometer at room temperature at a 4 cm^{-1} resolution in the range of 400–4000 cm^{-1}and the final spectrum was obtained averaging 32 scans.

DRIFT spectra were recorded with a Thermo spectrometer 4700 (400 scans with a resolution of 4 cm^{-1}) in the range of 600–4000 cm^{-1}.

UV-Vis spectra were recorded and collected by a JASCO V-350 spectrophotometer equipped with tungsten and deuterium lamps for visible and UV light analysis, respectively.

Photoluminescence (PL) spectra were measured with a JASCO FP-8200 fluorescence spectrometer equipped with of 150 W xenon lamp as the excitation source.

The relative quantum yields (QYs) of the CQDs were calculated according to a literature method [33]. As reference standard fluorescein (1 x 10^{-7} M in 0.1 M aqueous NaOH (pH 9.6)) was chosen. Fluorescein has a QY of approximately 86% at λ = 366 nm and λ =

313 nm. The UV absorbance of the samples was adjusted to be below 0.02 to minimize the inner filter effect.

The QY was calculated by the following equation:

$$QY_s = Q_r\left(\frac{A_r}{A_s}\right)\left(\frac{E_s}{E_r}\right)\left(\frac{\eta_s}{\eta_r}\right)^2$$

Where subscribers “r” and “s” refer to the fluorescein (reference) and evaluated sample, respectively. “QYs” stands for the quantum yield of the sample, “E” stands for the integrated PL intensity, “A” stands for the absorbance, and “η”stands for the refractive index of the solvent. Fluorescein (quantum yield: 86%) was dissolved in 0.1 M NaOH (refractive index: 1.33) and the C-dots were dissolved in water (refractive index: 1.33). The QY was measured at an excitation wavelength of 366 nm.

Textural characteristics (surface area, pore volume and pore diameter) were determined from the adsorption-desorption isotherms of nitrogen at -196 °C using a Micromeritics ASAP 2020 Surface Area and Porosity Analyzer.

Elemental analysis was made with an elemental analyzer EUROVECTOR EuroEA 3000.

TG-DTA analyses were recorded using a Shimadzu apparatus in a Pt crucible. The heating rate was of 10°C min^{-1}, respectively, starting from room temperature till 850 °C under a nitrogen flow of 50 mL min^{-1}.

Transmission electron microscopy (TEM) was performed on an electron microscope, Titan G2 60-300 kV FEI Company, equipped with field emission gun (FEG), monochromator, three condenser lenses system, the objective lens system, image correction (Cs - corrector), HAADF detector. The EDS spectrometer (Energy Dispersive X-Ray Spectroscopy) EDAX Company with Si (Li) detector was used to display the prepared samples. Microscopic studies of the samples were carried out at an accelerating voltage of the electron beam equal to 300 kV.

The mapping was carried out in the STEM mode by collecting point by point EDS spectrum of each of the corresponding pixels in the map. The collected maps were presented in the form of a matrix of pixels with the color mapped significant for element and the intensity corresponding to the percentage of the element.

2.4 Catalytic tests

The photocatalytic efficiency of the prepared CQD@TiO_2 samples was evaluated in methylene blue (MB) dye adsorption and degradation under visible light irradiation. Photocatalytic activity tests were performed in a cylindrical quartz photoreactors and blue LED lamps (112W), emitting at 445-465 nm, were used as light source.

In a typical experiment, 7.5-15 mg of photocatalyst was added to 10 ml of MB aqueous solution (30 mg/L). Before the photocatalytic degradation, the suspension was magnetically stirred in the dark, for 15 min, to establish the adsorption–desorption equilibrium of MB. Subsequently, the solution was irradiated with blue or red LED lamp and aliquots of 2.5 mL were collected from suspension at certain time intervals (10 min) and filtered using a 0.22 μm filter membrane. The concentration of MB after illumination was determined by a UV-vis spectrometer (SPECORD 250 - 222P108). The intensity of the main absorption peak (666 nm) of the MB dye was referred to as a measure of the residual MB dye concentration. Control experiments with pristine P-TiO_2 and M-TiO_2 were also performed.

For calibration curve stock solution of 500 mL with a concentration of 30 mg/L was prepared (15 mg MB dissolved in distilled water in a volumetric flask). The stock solution was used to prepare other five different MB concentrations as: 5, 10, 15, 20 and 25 mg/L. For each concentration the UV-vis spectra was registered (Figure 4A) and the corresponding absorbance value for the 666 nm band was used to build the calibration curve (Figure 4B). The calibration curve presents a linear relation and relationship coefficient was 0.9515 (Figure 4B).

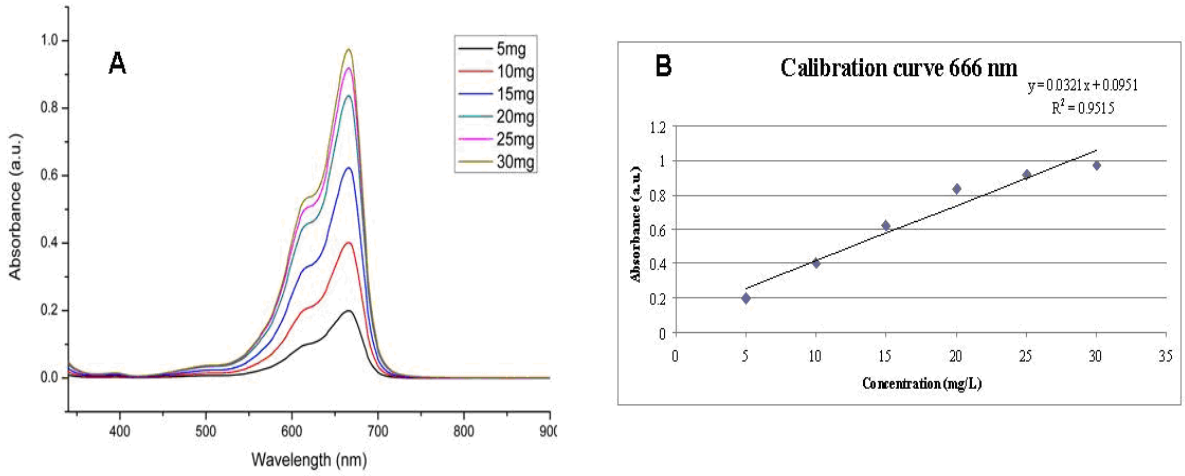

Figure 4. UV-vis band (665 nm) of MB at different concentrations (A) and calibration curve (B)

The MB conversion was defined as follows:

$$Conversion\ (\%) = \frac{C_0 - C}{C_0}\ x\ 100$$

where C_0 is the initial concentration of MB and C is the concentration of the MB at a certain reaction time, respectively.

Chapter 3. RESULTS AND DISSCUTION

3.1 Characterization of CQDs

The reaction time and temperature are the key factors in the hydrothermal approach preparation of CQDs. To probe the chemical composition of CQDs, prepared at different reaction times and different reaction temperatures, ATR-IR measurements were performed.

As Figures 5 A, B and C show the chemical composition differs only slightly from sample to sample. Therefore, for the as-prepared CQDs, the main bands identified in IR spectra can be associated to C=O stretching (1730 cm^{-1}) indicating the presence of acid, aldehyde, and ketone groups in their composition. The absorption band at 1370 cm^{-1} is attributed to the O-H in-plane deformation vibration or CH_x (x = 2, 3) bending vibration. The peaks at 2837 and 2939 cm^{-1} are assigned to the CH_x (x = 2, 3) stretching vibrations. The absorption bands at 1230 and 1100 cm^{-1} are ascribed to the C-O-C stretching of the furan ring deformation. The wide strong absorption bands centered at 1640, 2062, and 3300 cm^{-1} are mainly attributed to the water molecules. However, the 1640 cm^{-1} peak may also be partially contributed by the C=C stretching vibration of numerous sp^2 structures that enriched the aromatic structure, in agree with Weckhuysen and co-workers [10].

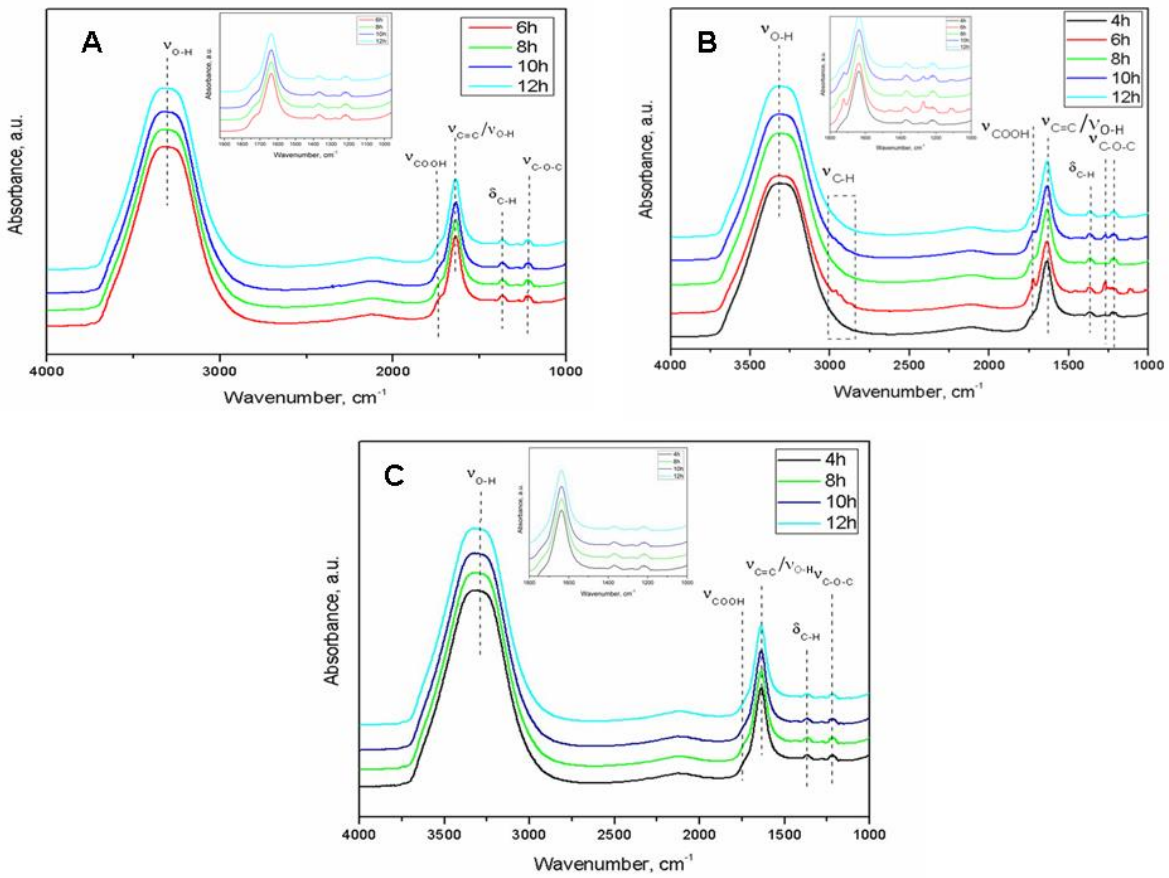

Figure 5. IR spectra on 1000-4000 cm^{-1} range of the CQDs synthesized at 160°C (A), 180°C (B) and 200°C (C) at different reaction times (insets: IR spectra on 1000-1800 cm^{-1} range)

The infrared spectrum of the CQDs shows similar features, except that the C=O absorption at 1730 cm^{-1} diminishes substantially when the hydrothermal temperature increased at 200°C. Such a variation supports the aforementioned speculation of the suppression of the C=O bonds with the hydrothermal parameters or their post-treatment [34]. Nevertheless, all synthesized CQDs are well dispersed and stable in water for a long period of time (several months) indicating the existence of a high concentration of the hydroxyl groups on their surface, irrespective of the synthesis conditions, in agree with literature reports [34; 35].

In the XRD pattern of $CQD_{200\text{-}4}$ (Figure 6) two diffraction lines centered at 22^0 and 42^0 are evidenced, indicating that a graphite-like structure existed in their carbon core. However, $CQD_{180\text{-}12}$ displays a broad line centered at 24^0 that is attributed to highly disordered graphitic carbons (JCPDS 26-1076) [35]. Moreover, the lower line intensity along with a relatively higher full width half maximum, indicate a smaller size of the $CQD_{180\text{-}12}$ sample [34].

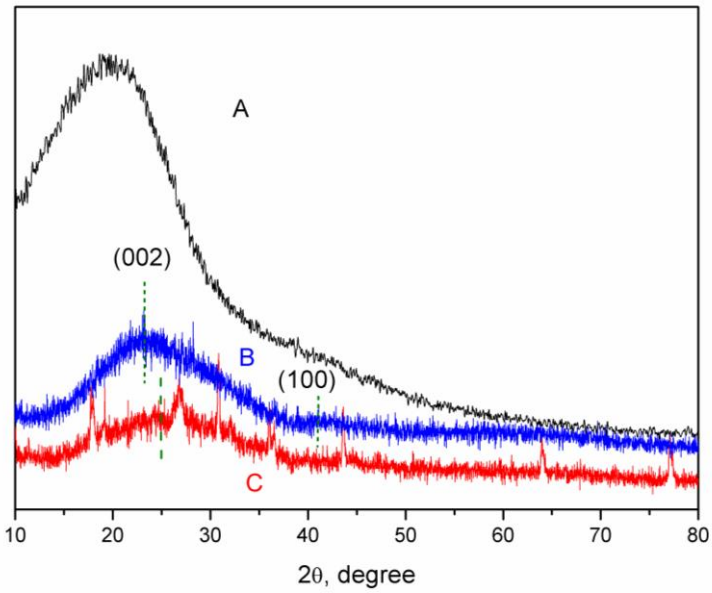

Figure 6. XRD pattern of the humins (A), $CQD_{200\text{-}4}$ (B) and $CQD_{180\text{-}12}$ (C)

In quest of exploring the spectral properties of the as-prepared CQDs, the UV-Vis absorption and PL spectra were acquired. Figures 7-9 shows the PL spectra of as-prepared CQDs aqueous solutions, excited at various λ_{ex}.

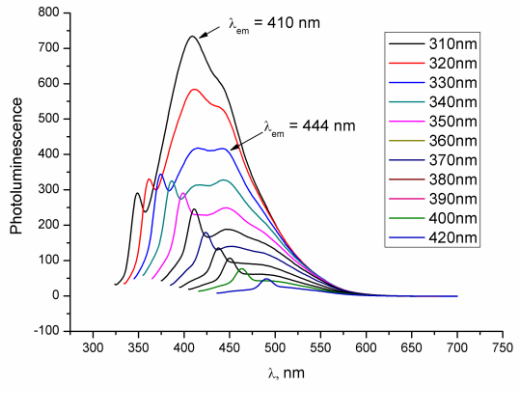

Figure 7. PL spectra of $CQD_{180\text{-}4}$ with λ_{ex} of 310-420 nm

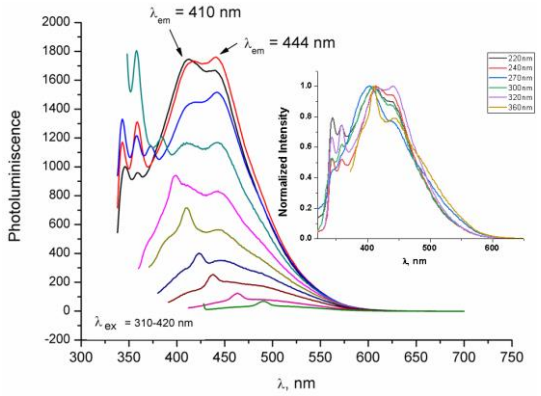

Figure 8. PL spectra of $CQD_{180\text{-}12}$ with λ_{ex} of 310-420 nm (inset: PL spectra with normalized intensity, λ_{ex} of 220-360 nm)

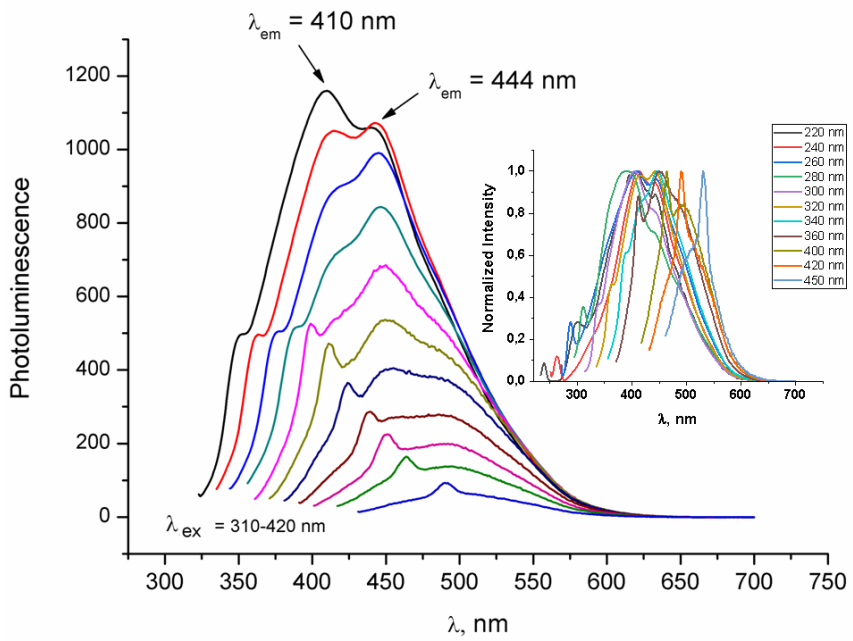

Figure 9. PL spectra of $CQD_{200\text{-}4}$ with λ_{ex} of 310-420 nm (inset: PL spectra with normalized intensity, λ_{ex} of 220-450 nm)

The broad and irregular emission peaks suggest that the fluorescence of CQDs derived from different surface functional groups or/and carbon core structure. The typical PL spectra comprise two fluorescence emission centers: one indigo-blue centered at around 410 and another blue peak centered at 444 nm. Also, some sharp violet peaks centered at below 400 nm are observed. The relative intensity of the indigo-blue emission (410 nm) decreases while that of the blue emission (444 nm) increases with increasing excitation wavelength. These contrary variation trends also suggest their different origins. However, both fluorescence emission centers are located at 410 and 444 nm without any perceptible excitation dependence when the λ_{ex} was less than 360 nm (inset Figures 7 and 9). When λ_{ex} moves from 360 to 450 nm a distinct red-shift in the emission wavelength of the $CQD_{200\text{-}4}$, from 445 nm to 530 nm, was observed (Figure 9). The same shifts were also observed in the case of $CQD_{180\text{-}12}$ sample (not shown in Figure 8).

The excitation-dependent PL behavior is usually attributed to the various size distributions (quantum effect) [36] that make the difference in optical selection, and to the presence of the oxygen-containing functional groups, which affected the band gap of CQDs [37]. On the other hand, the excitation-independent PL behavior derived from the homogeneous particle size, in agree with literature reports [38], but the high polarity of nanosized cluster and the sp^2-carbon networks is claimed as being responsible for excitation-dependent PL behavior [39].

Taking into account this information and on the base of the obtained results, we can assume the formation of CQDs with preponderantly homogeneous particle with small size, for which the emission is due to the intrinsic luminescence of the sp^2-carbon networks which is responsible for the shorter wavelength part of emission (excitation-independent; λ_{ex} = 250-340 nm, λ_{em} =445 nm). However, the excitation-dependent behavior of the longer wavelength part (λ_{ex} = 340 - 450 nm, λ_{em} = 445-530 nm) indicate the formation of some nanoclusters with bigger size with a similar behavior as those formed by the aggregation of single CDs in high concentrated solution, claimed by Yang et al. [40]. In both cases it results a larger number of –CO and –OH get together, which leads to the higher polarity on the surfaces of nanoclusters. This high polarity leads to electron rapid relaxation from excited states to substates, which corresponds to longer wavelength. Then, the substates contribute to photo emission, which eventually gives rise to longer wavelength emission [41].

The irregular shape of the PL spectra of the $CQD_{180\text{-}12}$ sample may indicate either the existence of different fluorophore or/and the presence of impurity states. In order to check the origin of these emissions part of CQD_s sample were washed with dichloromethane and the PL spectra of the obtained sample ($CQD_{180\text{-}12S}$) were again analyzed (Figure 10).

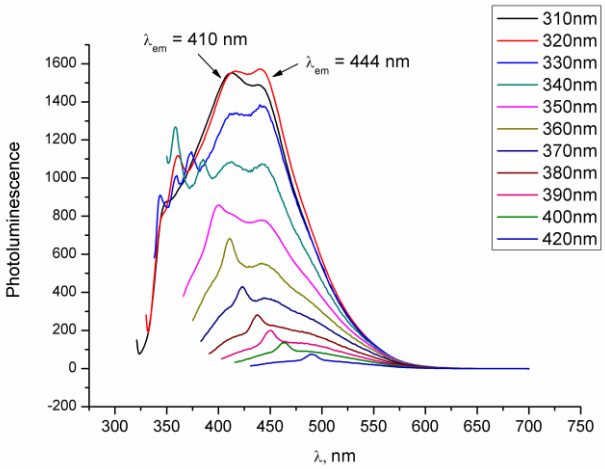

Figure 10. PL spectra of the $CQD_{180\text{-}12S}$ sample with λ_{ex} of 310-420 nm

Comparing the PL spectra of $CQD_{180\text{-}12}$ (Figure 8) and $CQD_{180\text{-}12S}$ (Figure 10), some of sharp violet peaks centered at below 400 nm vanished after washing with dichloromethane. Remained peaks are similar with those observed in the other samples but with a higher intensity indicating the presence of fluorophore oxygen-containing functional groups in a higher amount on this sample, in agree with IR results.

The highest fluorescence emission is obtained at around 444 nm for an excitation at 320 nm (Figures 7-9). Therefore, in order to display the effect of hydrothermal parameters on the fluorescence characteristics of CQDs, their emission spectra (λ_{ex} = 320 nm), at hydrothermal temperatures of 180-200°C and 4-12h, were compared (Figure 11).

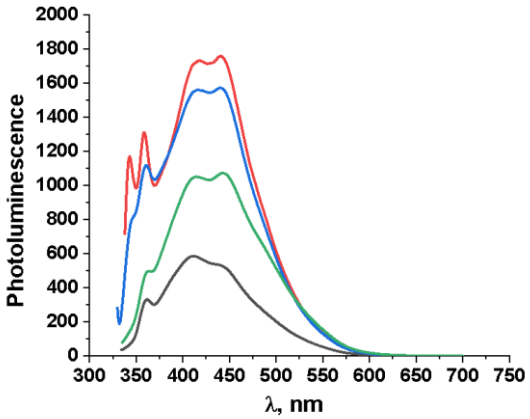

Figure 11. The PL spectra comparison for $CQD_{180\text{-}4}$ (black), $CQD_{200\text{-}4}$ (green), $CQD_{180\text{-}12S}$ (blue) and $CQD_{180\text{-}12}$ (red) samples (λ_{ex} = 320 nm).

As Figure 11 shows both synthesis parameters affect the formation progress of quantum dots and their fluorescence properties. The highest PL intensities are displayed for $CQD_{180\text{-}12}$ followed by $CQD_{180\text{-}12S}$, $CQD_{200\text{-}4}$ and $CQD_{180\text{-}4}$ sample.

Clearly enough, the fluorescence intensity is highly dependent by the reaction time (Figure 11, $CQD_{180\text{-}4}$ (black) and $CQD_{180\text{-}12}$ (red)). This dependence suggests an increase in the carbon dot concentration with reaction time. However, $CQD_{200\text{-}4}$ displays an increased luminescence intensity than $CQD_{180\text{-}4}$ but longer reaction time (i.e., in excess of 4 h) causes a decrease in the luminescence intensity (not showed in Figure 11). This signifies that a long reaction time for high temperatures result in the formation of carbon particles with larger size due to the aggregation, which do not exhibit fluorescence.

On the other hand, it was shown that the surface status of CQDs markedly affects their PL properties [42]. For amorphous CQDs, the surface status is mainly affected by the number and type of the functional groups on the surface [43]. Hence, the PL properties of the amorphous $CQD_{180\text{-}12}$ were mainly determined by their surface groups. Indeed, IR results indicated that the $CQD_{180\text{-}12}$ contained more carboxyl acids and hydroxyl groups, which could act as radiative recombination centers and introduce more defects at their surface, leading to stronger fluorescence emission. In comparison, the $CQD_{200\text{-}4}$ had more epoxy and ether

groups, which acted as non-radiative recombination centers and resulted in the weaker fluorescence emission.

Additionally, when λ_{ex} was 366 nm, the calculated QYs of these samples varies from 8% (CQD_{180-4}) to 15% (CQD_{200-4}) to 21% (CQD_{180-12}), respectively. The QY of the $CQD_{180-12S}$ slightly decreases to 20% by comparing with the CQD_{180-12}. Zhu and co-workers [51] showed not long ago that CQDs exhibit a higher PL intensity after surface reduction but no obvious emission shift, which shows that the QY of CQDs is controlled by the surface chemistry. Obtained values are in line with those reported in literature [38].

C-dots prepared by typical methods usually show strong ultraviolet (UV) absorption, but the positions of UV absorption peaks of C-dots prepared by different methods are quite different [44]. The UV-Vis absorption features of the CQDs produced in this work were examined and the detailed results are given in Figure 12. The inset in Figure 12 shows the images of the CQD_{200-4} solutions taken under visible and ultraviolet light of 365 nm wavelength, which demonstrate a faint yellow color under visible light and emit a distinct blue light under UV light.

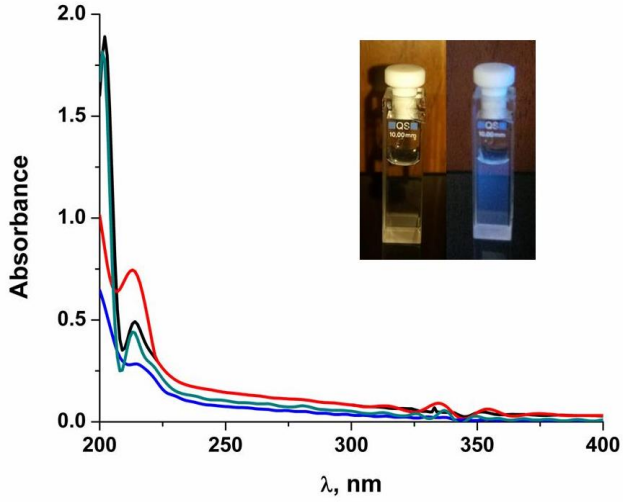

Figure 12. The UV-Vis absorption spectra for $CQD_{180-12S}$ (black), CQD_{180-12} (green),CQD_{180-4} (blue), and CQD_{200-4} (red) samples

Similar to the previous studies in CQDs and GQDs [48-56], the absorption peaks in shorter wavelength can be ascribed to π -π* transition of aromatic C=C bonds in sp^2 hybrid domains while and the shoulders at longer wavelength are attributed to n– π* transition of C=O or C-OH bond in the sp^3 hybrid region. However, it is clearly the nature of C=C bonds are different in CQD_{180-12} and CQD_{200-4} samples with a more disordered structure in the CQD_{180-12} sample. When samples are illuminated by 365 nm light, the CQDs solutions emit

an intense blue color which indicates that the PL emission wavelength (λ_{em}) was red-shifted (the inset in Figure 12).

Based on the above results it can be stated that the CQDs structure retains the spherical core-shell morphology of the humins raw materials. However, both the core and shell have different structures as a function of the hydrothermal reaction conditions. Therefore, for a high temperature and a short reaction time CQDs with a graphite-like structure of the core and a shell which had more epoxy and ether groups along hydroxyl groups ($CQD_{200\text{-}4}$) are obtained while for lower temperature and a longer reaction time CQDs with an amorphous structure of the core and a shell which contained more carboxyl acids along hydroxyl groups ($CQD_{180\text{-}12}$). However, the difference in the core size is not high enough both kinds of CQDs emitting in blue light. A general schematic illustration of the spherical core-shell morphology of CQDs obtained in this work is given in Scheme 2.

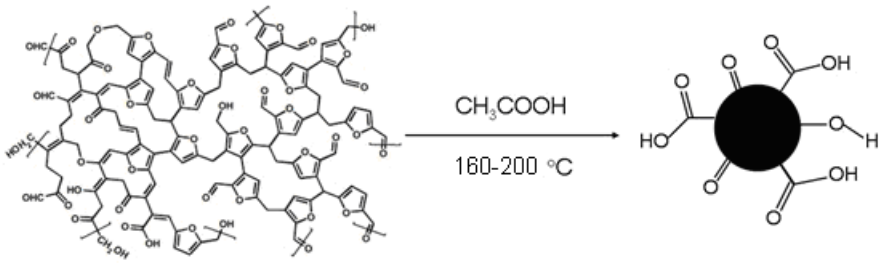

Scheme 2. Schematic illustration of the spherical core-shell morphology of CQDs obtained by hydrothermal treatment of humins

3.2 Characterization of CQD@TiO_2 nanocomposites

The XRD patterns of P-TiO_2, M-TiO_2 and CQDs@TiO_2 are given in Figures 13A, B and C. The lines at 25.3°, 37.8°, 48.1°, 54.0°, and 62.7° are attributed to (101), (004), (200), (105), and (204) crystal planes of anatase TiO_2 (JCPDS card 21-1272) [46], while the lines at 27.4°, 35.9, 54.9 and 68.8° are attributed to (110), (101), (211) and (301) reflection of rutile TiO_2, respectively (Figure 13A) [47]. No diffraction lines at 29.8 and 44.4◦, corresponding to those of brookite TiO_2 phase (JCPDS 74-1940) were identified [48].

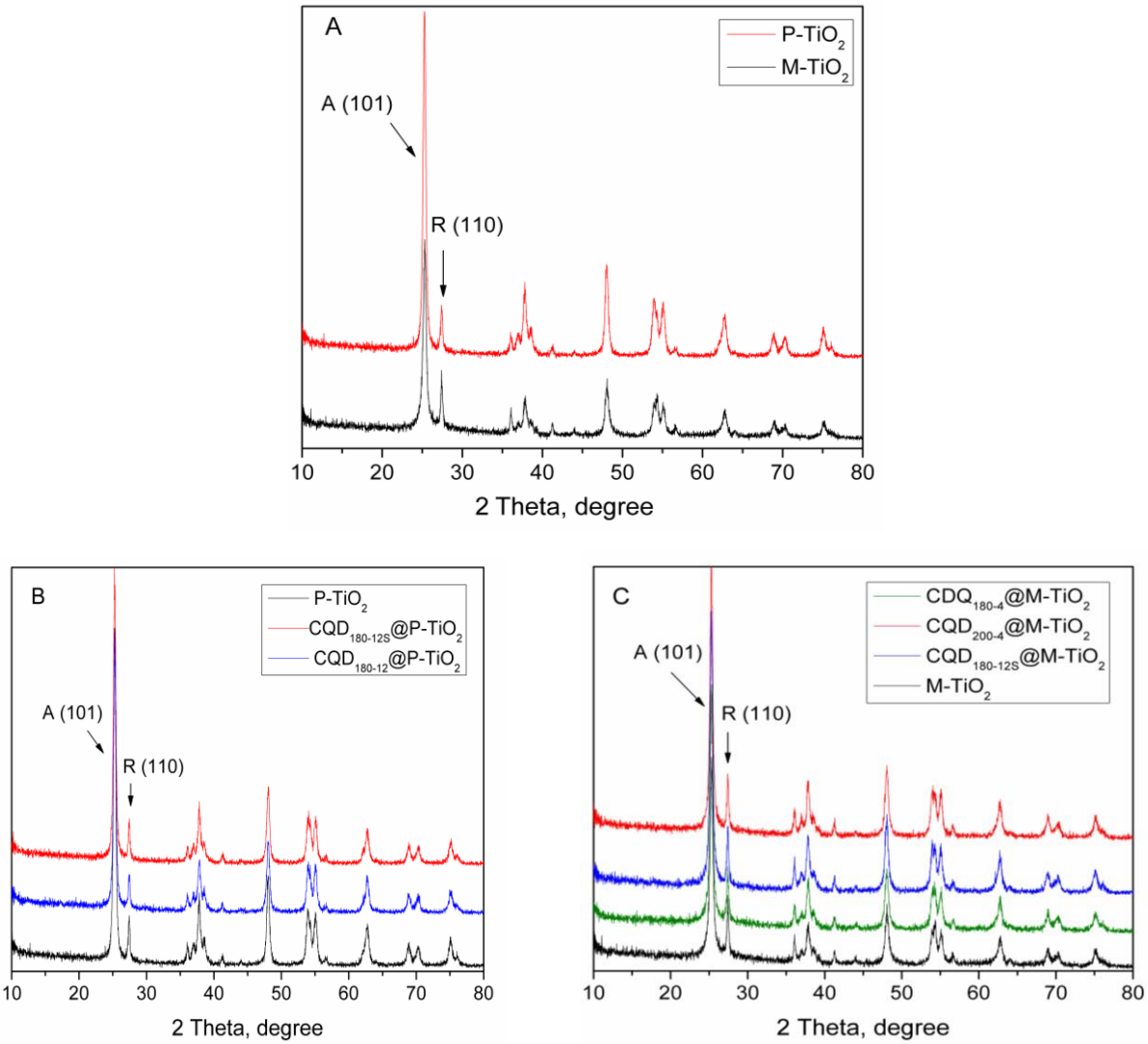

Figures 13. XRD patterns of P-TiO_2 and M-TiO_2 carriers (A), CQD@P-TiO_2 (B) and CQD@M-TiO_2 (C) samples

Lines at 2θ = 25.30° and 27.40° (indicated with arrows in Figures 13A-C) are often taken as the characteristic lines of anatase (101) and rutile (110) crystal phase, respectively [49]. The mass percentage of anatase and rutile phases in the TiO_2-based materials is estimated from the respective integrated characteristic XRD lines intensities [50]:

$$Anatase\,(\%) = \frac{100}{1 + 1.265\frac{I_R}{I_A}} \qquad Rutile\,(\%) = 100 - Anatase\,(\%)$$

where I_R and I_A represent the lines intensities of (101) and (110) reflections for anatase and rutile, respectively; 1.265 represent the quality factor ratio of anatase to rutile.

The average size of crystallites was determined from using the reflection (101) of anatase and the Debye-Scherrer equation [49]:

$$d = \frac{k\lambda}{\beta \cos\theta}$$

where d is the crystallite size in nm; k = 0.94; λ is the wavelength of the X-ray (1.54178 Å); θ is the half-diffraction angle and β is the full width at half-maximum (FWHM) in radians for the 2θ value (25.3°).

As Figure 13A shows, the rutile content in the M-TiO_2 increased at the cost of anatase phase. Therefore, if P-TiO_2 sample is composed of 84.5% anatase TiO_2 and 15.5% rutile TiO_2, the M-TiO_2 is composed of 72% anatase and 28% rutile TiO_2.

However, the CQDs@TiO_2 samples exhibit identical patterns with the corresponding TiO_2 carrier (i.e., P-TiO_2 or M-TiO_2) without diffraction lines shifting. This demonstrates that the crystal structure of TiO_2 was not modified by the CQDs (Figures 13B and 13C). In other words, the CQDs were just well deposited on the surface of the TiO_2 and not incorporated into its lattice [50]. Moreover, the XRD patterns of the CQD@TiO_2 samples (Figures 13B and C) did not evidence diffraction lines characteristic to CQDs, indicating their small loading weight, poor crystallinity, small size and/or their high dispersion in the CQD@TiO_2 composites [51]. The average crystallite sizes, calculated with Debye-Scherrer equation, slightly vary in the range of 18.3 (M-TiO_2) - 20.0 (P-TiO_2) nm with CQD@TiO_2 inside these limits, indicating that such composites powders are made up of nanocrystalline particles.

The presence of CQDs in the CQD@TiO_2 nanocomposites was confirmed by the elemental analysis (Table 3) and TG-DTA analysis (Figure 14).

As Table 3 shows, the contents of C and H, derived from CQDs, varies in ranges of 1.1-4.2% and 0.3-1.3%, respectively, indicating different weight loadings of CQDs on the titania carrier.

Table 3. The C and H content in CQD@TiO_2 determined by elemental analysis

Sample	**$CQD_{180\text{-}4}$ @M-TiO_2**	**$CQD_{180\text{-}12S}$ @M-TiO_2**	**$CQD_{200\text{-}4}$ @M-TiO_2**	**$CQD_{180\text{-}12S}$ @P-TiO_2**	**$CQD_{180\text{-}12}$ @P-TiO_2**
C (%)	4.162	2.564	2.111	2.188	1.065
H (%)	1.329	0.878	1.127	0.638	0.334

The thermogravimetric/differential thermic analysis (TG/DTA) also confirms the successful deposition of the CQDs. In Figure 14 the TG/DTA profiles for $CQD_{180\text{-}4}$@M-TiO_2

and $CQD_{200\text{-}4}$@M-TiO_2 sample are given for exemplification, together with the TG/DTA profiles of M-TiO_2 and humins, for comparison

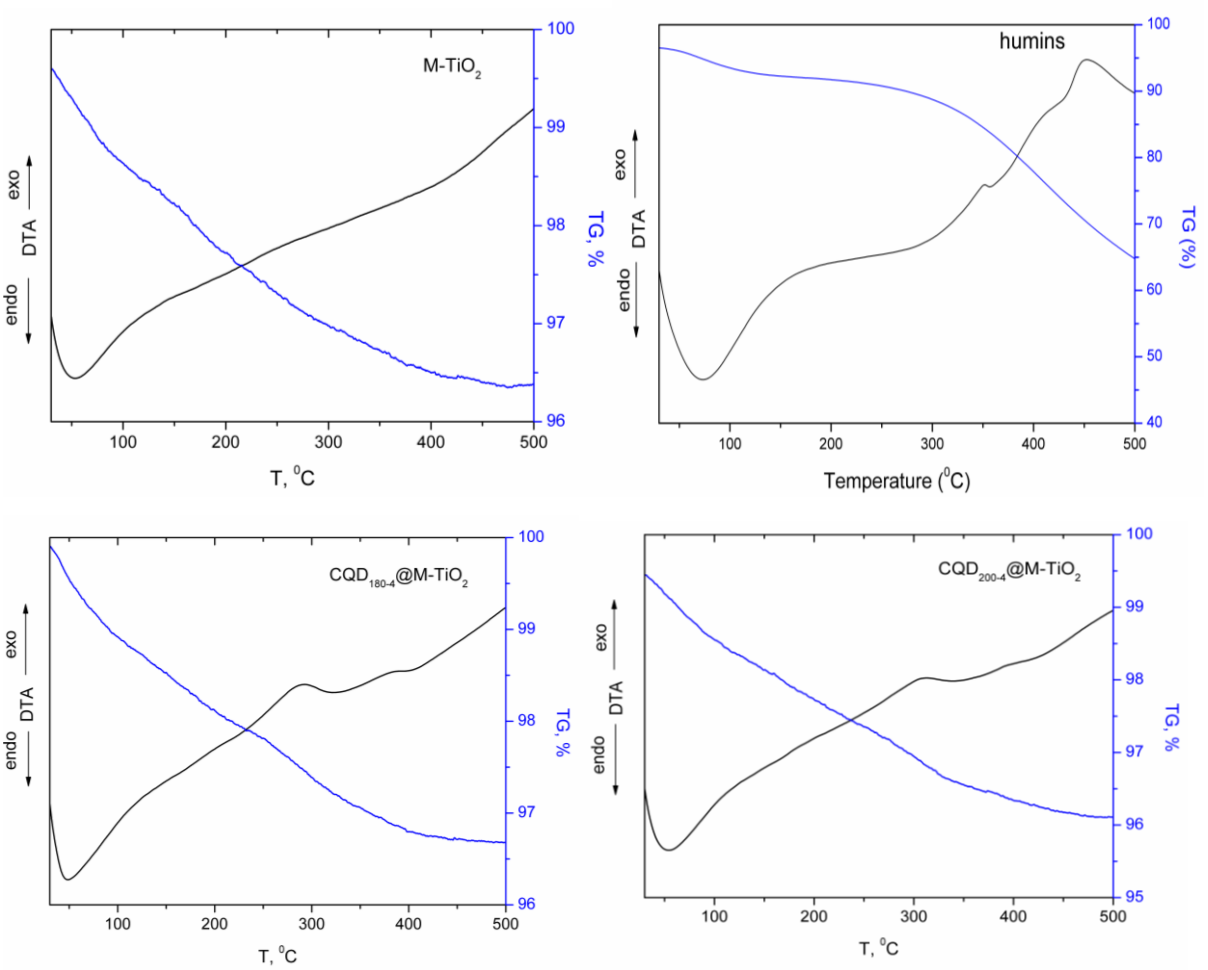

Figure 14. TG-DTA profiles of M-TiO_2, humins, $CQD_{180\text{-}4}$@M-TiO_2 and $CQD_{200\text{-}4}$@M-TiO_2 samples

As Figure 14 shows the DTA profile of all samples showed an endothermic effect at around 50-60°C, that is associated to a weight loss assigned to physically adsorbing water. However, in the case of CQD@TiO_2 samples other two exothermic effects, with maxima at 300 and 385°C, respectively ($CQD_{180\text{-}4}$@M-TiO_2 sample) and at 310 and 400°C, respectively ($CQD_{200\text{-}4}$@M-TiO_2 sample) are observed. Even if the loss weight cannot be quantitatively appreciated, the presence of these effects can be attributed to different decomposition processes which take place at high temperature, such as dehydroxylation, decarboxylation, and decarbonylation, indicating the presence of CQDs in CQD@M-TiO_2 samples. Such processes lead to the formation of a relative stable polycyclic aromatic structure, in accordance to previous literature reports [30].

The structural modifications in the M-TiO_2 sample were evidenced by TEM analysis (Figure 16). For comparison, the TEM imagines for the P-TiO_2 sample, with a similar magnification, are also presented in Figure 15.

TEM images of the P-TiO_2 powder (Figure 15) reveals lattice fringes of anatase and rutile stacked in the direction (101) and (110), respectively, indicating that the anatase and rutile particles exist separately, but in close proximity, by forming their agglomerates [25]. Also, the coexistence of (101) plane of anatase and (110) plane of rutile indicates the formation of mixed-phase TiO_2-based junctions. The combination of the anatase and rutile phases of P-TiO_2 exhibits higher photocatalytic performance in the decomposition of various organic pollutants than that of pure anatase or rutile phase due to the transfer of electrons from rutile to anatase TiO_2 across the junction interface, which inhibits the charge recombination of anatase, leading to more efficient separation of the photogenerated electron–hole pairs and greater photocatalytic activity [52]. However, photocatalytic activity of P-TiO_2 is still restricted by the small specific surface area and limited surface reaction sites [25].

When P-TiO_2 was hydrothermal treated with concentrated aqueous NaOH solution, followed by washing with HCl and subsequent calcination at 450°C, unexpected nanoparticle/nanotube hybrid nanostructures were obtained, as TEM imagine shows (Figure 16). During the hydrothermal treatment of the P-TiO_2 sample with aqueous NaOH solution some Ti-O bonds of the TiO_2 precursor are broken, leading to the formation of lamellar fragments, with a two-dimensional layered structure, that are the intermediate phase in the formation process of the nanotube material [31; 32]. However, while some studies showed that the condition of the post-treatment washing affected the formation, crystalline structure, or even chemical composition of the final products [53], some other studies claimed that nanotubes were formed during the NaOH treatment, and that the acidic post-treatment was not essential in their synthesis [54]. Moreover, a comparison of the microstructures between the products with and without a post-treatment with HCl indicated that the acidic treatment did not enhance the formation of the nanotubes, but introduced many defects on the nanotubes instead [55].

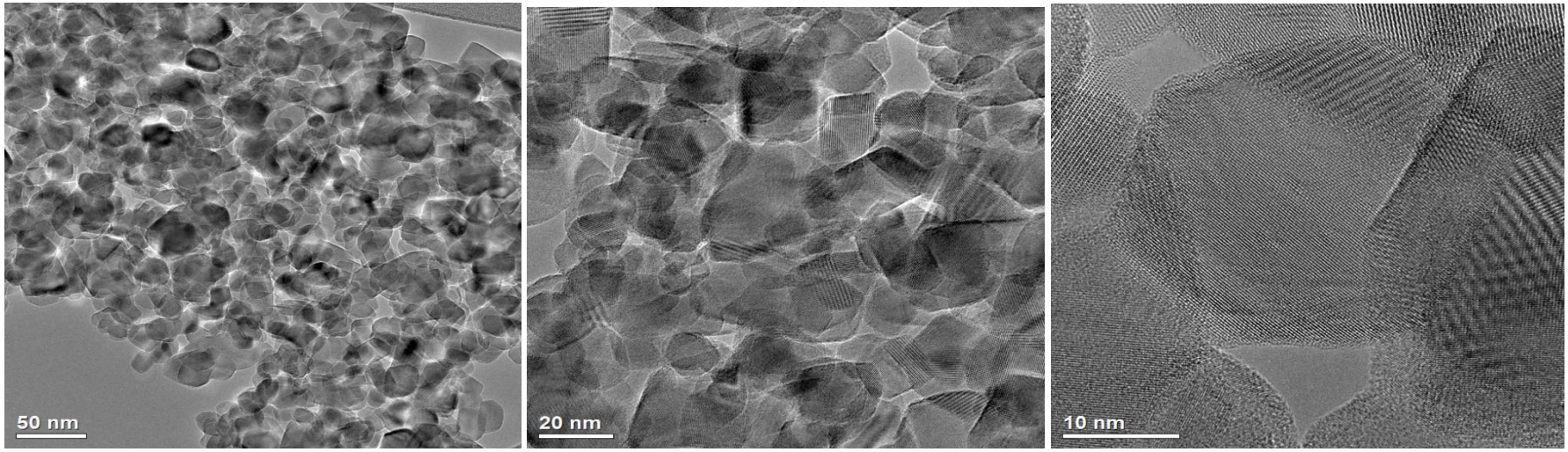

Figure 15. TEM images of P-TiO_2 sample

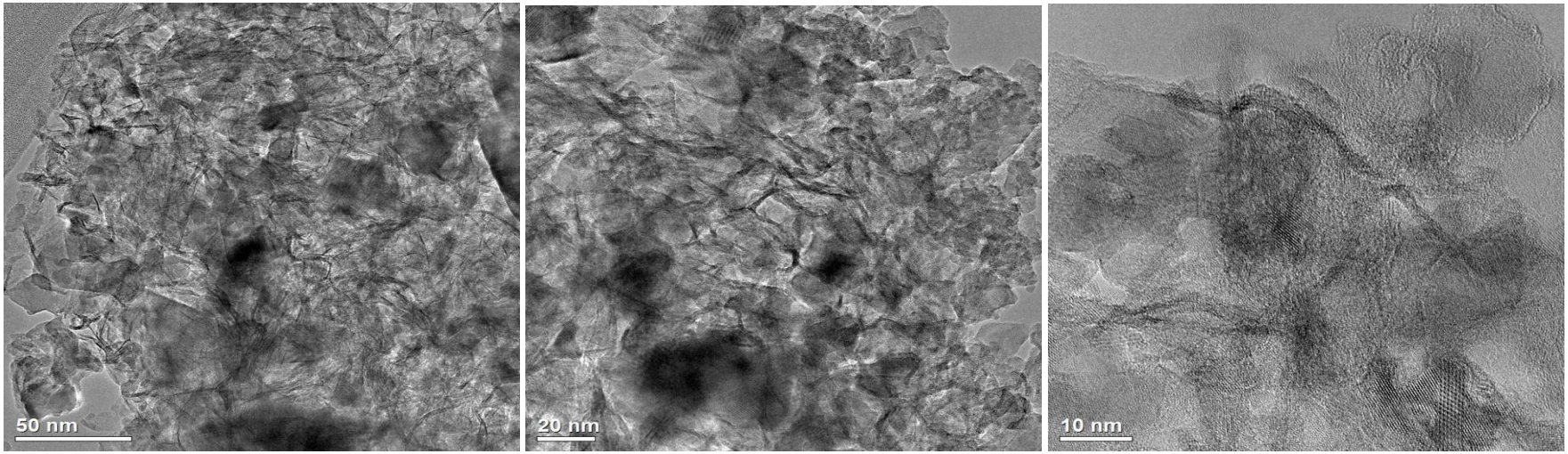

Figure 16. TEM images of M-TiO_2 sample

Considering the crystalline characteristics of anatase (a = b ≅ 3.78 Å; c ≅ 9.52 Å) and rutile (a = b ≅ 4.59 Å; c≅ 2:95 Å) phase, Seok et al [56] deduced that anatase (with longer c axis) rather than rutile one is preferred to form the nanotube. Also, theoretical studies [57] suggested that the surface energy of anatase TiO_2 macroscopic crystal is smaller than that of rutile phase. This can also explain the fact that TiO_2 nanotubes are preferred to have the anatase structure. These findings are consistent with the increased diffraction line intensity of rutile TiO_2 in the XRD measurements (Figure 13A). Also, according with the TEM image of M-TiO_2 (Figure 16), TiO_2-based heterophase junction, with three mixed phases of anatase and rutile nanoparticles but also anatase nanotubes has been successfully prepared. The existence of these phases and their intimate contact is considered to facilitate interfacial charge transfer in a higher degree than P-TiO_2. Moreover, the acidic post-treatment and the subsequent heat-treatment procedure will generate oxygen vacancies in the mixed-phase junctions enhancing the adsorption and uniform dispersion of the reactant in photocatalytic degradation of dyes. Due to the enhanced charge separation around heterophase interfaces and the decreased charge transfer resistance, as-synthesized oxygen-deficient heterophase junctions should also exhibit significantly improved activity for photocatalytic degradations.

The morphology of different samples was studied by STEM-EDS analysis. As shown in Figures 15 and 16, in P-TiO_2 (Figure 15) a large number of nanoparticles with the diameter in a range of 27-30 nm are observed, while M-TiO_2 (Figure 16) are composed of 1-D nanostructures, which are further self-assembled into a 3D fibrous network with adhered nanoparticles to the surface. Moreover, individual CQDs, with spherical-like shape nanoparticles and the diameter of 2-8 nm, can be observed on the surface of TiO_2. Obtained results confirm the different CQDs sizes as a function of the hydrothermal parameters (i.e., temperature and reaction time). Therefore, CQDs synthesized at 180°C and 12 h, possess a mainly size of 2 nm (Figure 17), while CQDs synthesized at 200°C and 4 h possess a main size of around 8 nm (Figure 18). Also, very important, their size is mainly homogenous, in agree with the PL results.

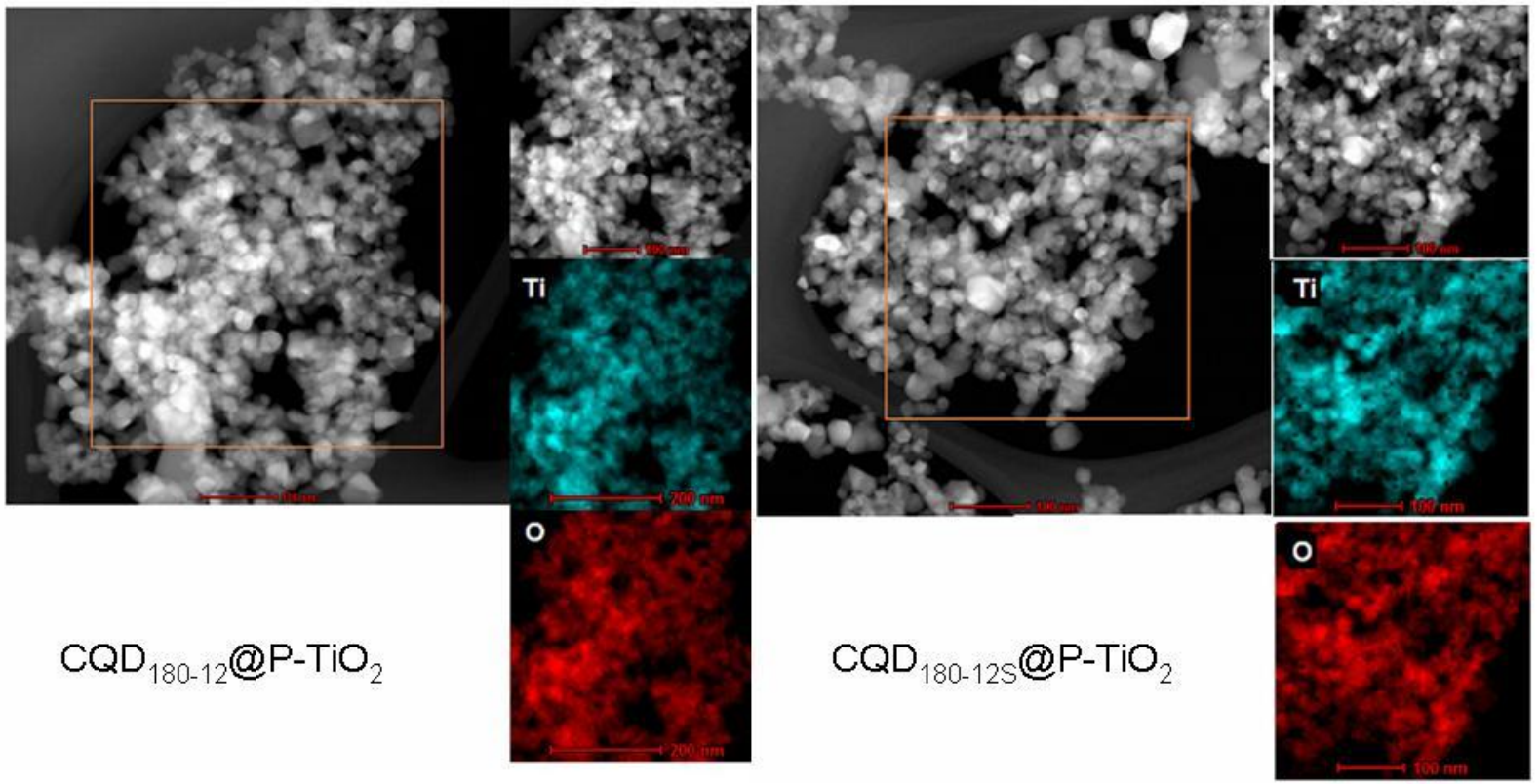

Figure 17. STEM images of CQD@P-TiO_2 samples

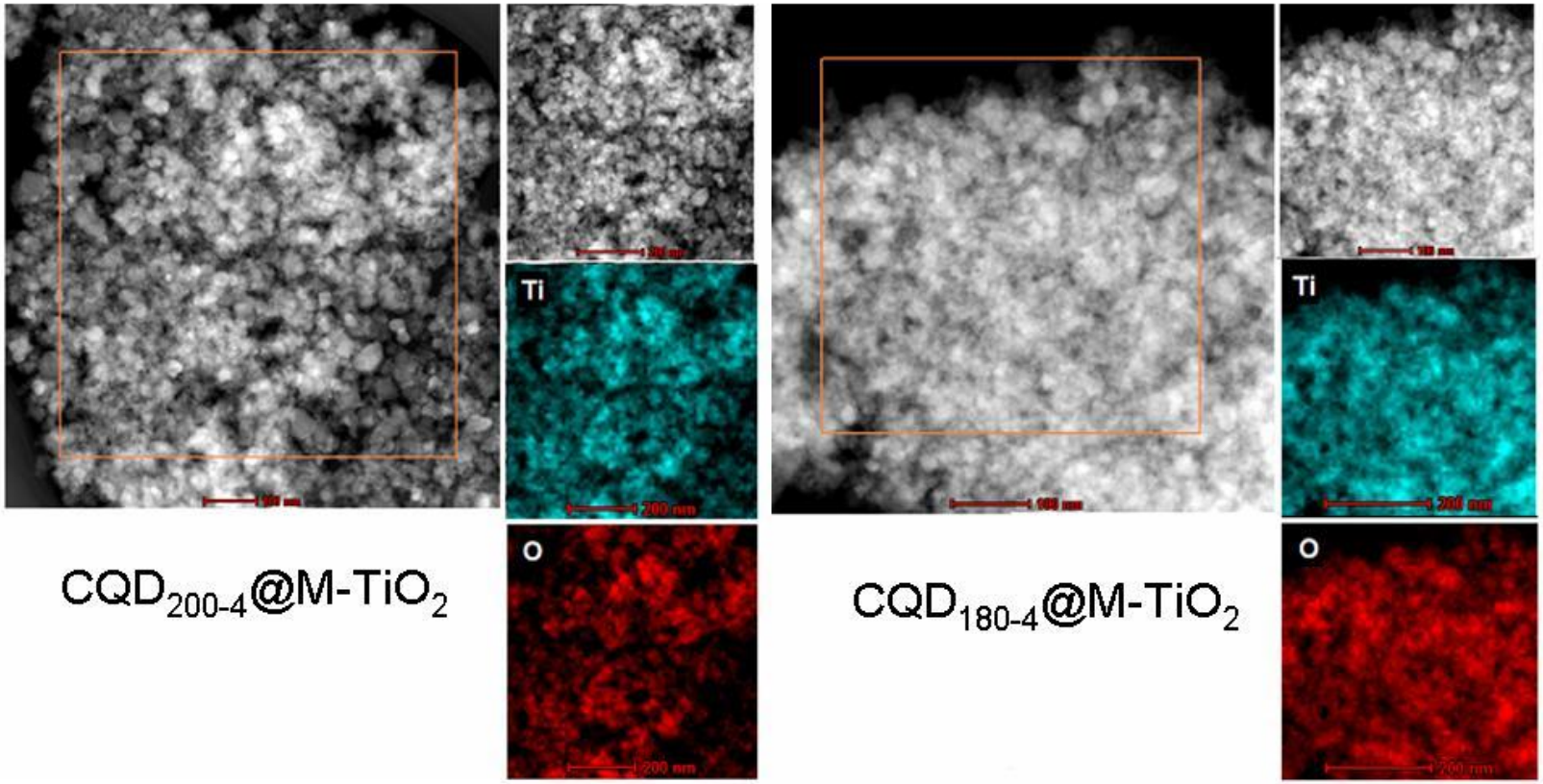

Figure 18. STEM images of CQD@M-TiO_2 sample

To discuss the chemical nature of the interaction between CQDs and titania carriers, CQDs@TiO_2 samples were further investigated by IR spectroscopy and obtained spectra were compared with titania carrier spectrum (Figure 19).

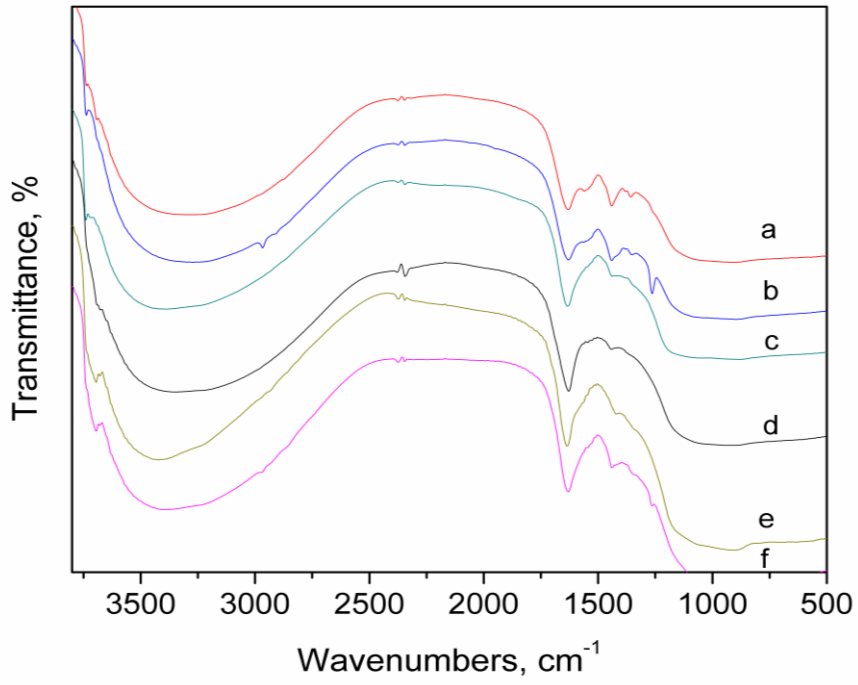

Figure 19. FT-IR spectra of the M-TiO_2 and CQD@TiO_2 nanocomposites: a. $CQD_{180\text{-}12S}$@M-TiO_2; b. $CQD_{200\text{-}4}$@M-TiO_2; c. $CQD_{180\text{-}4}$@M-TiO_2; d. M-TiO2; e. $CQD_{180\text{-}12}$@P-TiO_2; f. $CQD_{180\text{-}12S}$@P-TiO_2

The absorption bands at 3380 cm^{-1} are ascribed to the stretching vibration of the Ti-OH groups on the out-surface of the TiO_2 [58] which can capture the photoexcited electrons and holes to produce the reactive oxygen species in the photocatalytic process [59]. However, new distinct peaks at 3690 and 3740 cm^{-1} are evidenced after the decoration of TiO_2 with CQDs, which most probably belongs to CQDs.

The peak at 1620 cm^{-1} is corresponding to the surface adsorbed water molecules [60]. After surface modification with CQDs, the obvious change on the functional groups of TiO_2 was the appearance of two peaks at around 1380 cm^{-1} and 1270 cm^{-1}. These peaks were conjectured to be –COOTi– group, which originated from the esterification between the carboxyl groups from CQDs and the hydroxyls groups from TiO_2 (Scheme 3) [61]. In addition, strong hydrogen bonds could form between the hydroxyl groups from the surface of CQDs and TiO_2. All these results confirm that the CQDs and TiO_2 have a good chemical connection, forming a heteroconjunction system which enables photoexcited charge carriers to transfer through the contact interface.

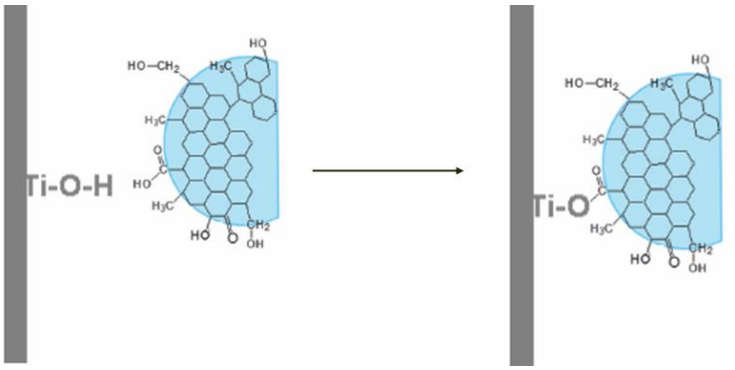

Scheme 3. Schematic representation of the esterification reaction between the carboxyl groups from CQDs and the hydroxyls groups from TiO_2

The Brunauer-Emmett-Teller (BET) surface area, pore volume, and pore size of the CQD@TiO_2 nanocomposites were determined by N_2 adsorption–desorption experiments. The isotherms are shown in Figure 20, while the insets show the Barrett-Joyner-Halenda (BJH) pore distribution.

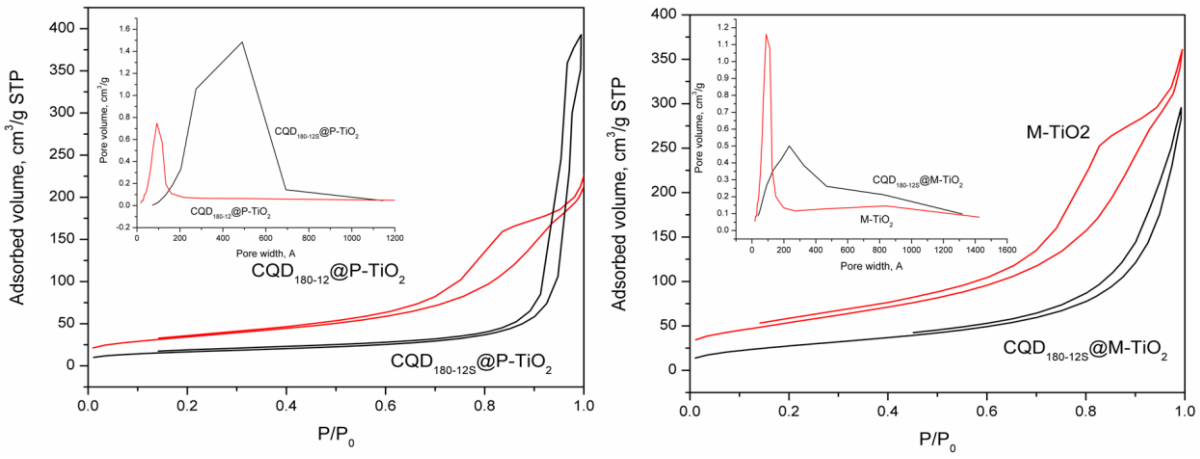

Figure 20. N_2 adsorption-desorption isotherms at 77 K for CQD@P-TiO_2 and CQD@ M-TiO_2 nanocomposites

The isotherm curves characteristic to samples presented in Figure 20 exhibit a distinct uptake of N_2 as a result of capillary condensation in a wide relative pressure (P/P0) range of 0.5–1.0 (H3 type hysteresis loop), which suggested the existence of a mesoporous structure (2-50 nm). However, the high-pressure hysteresis loop (0.8 < P/P0 < 1.0) characteristic for $CQD_{180\text{-}12S}$@P-TiO_2 is associated with the larger pores formed between secondary particles [42]. In the case of $CQD_{180\text{-}12S}$@P-TiO_2 there is also a bimodal pore size distribution

consisting of intra-aggregated pores with a maximum pore diameter of 27.1 nm and larger inter-aggregated pores with a maximum pore diameter of 49 nm (Table 4). According to Kumar et al. [62], the bimodal pore size distribution arose from the hard aggregated in the powders. In addition, there were two types of pores on the bimodal pore size distribution. One is the intra-aggregated pore (represented by the hysteresis loop in the lower *P*/*P*0 range) and the other is the larger inter-aggregated pore (hysteresis loop in the higher *P*/*P*0 range). For M-TiO_2 based samples (Figure 20, Table 4), the maximum pore sizes of the intra-aggregated pores shifted into larger mesopores regions (ca. 9.1 and 23.3 nm, respectively), indicating the growth of pores.

Table 4. BET surface areas, pore volumes and pore sizes of the CQD@TiO_2 nanocomposites

Entry	Sample	S_{BET}, m^2/g	V_p, cm^3/g	D_p, nm
1	P-TiO_2	54	0.31	19.7
2	$CQD_{180\text{-}12}$@P-TiO_2	123	0.33	8.7
3	$CQD_{180\text{-}12S}$@P-TiO_2	59	0.54	27.1 and 49.0
4	M-TiO_2	194	0.56	9.1
5	$CQD_{180\text{-}12S}$@M-TiO_2	203	0.45	23.3

As seen from Table 4 the BET surface areas of CQDs@P-TiO_2 (59 and 123 m^2/g) are larger than that of pure P-TiO_2 (54 m^2/g). The applied modification strategy of P-TiO2 material also leads to an increased BET surface area of the obtained M-TiO_2 sample (194 m^2/g) which further increased to 203 m^2/g, as a result of the CQDs insertion (Table 4, entry 5, $CQD_{180\text{-}12S}$@M-TiO_2 sample). These modifications are obviously due to both the structural modifications of M-TiO_2 and the presence of CQDs. The nanoparticles/nanotubes heterophase junction obviously results in an increased surface area. Moreover, when coupling CQDs with TiO_2 nanospheres/nanotubes, the CQDs anchored on the surface of TiO_2 increases its surface roughness, resulting in the formation of a second interface between CQDs and TiO_2.

The wide application of titanate nanosheets [44] or titanate nanotubes [45] as photocatalysts is limited by the fact that their band gaps are wider (3.87 eV for titanate nanotubes and 3.84 eV for titanate nanosheets) than that of TiO_2 particles (3.2 eV). The high increase is attributed to the quantization of electronic states in these materials and the reduction of dimensionality from 3-D to 2D and/or 1D [45]. However, as we already showed, in this work generated high surface and defects (oxygen vacancy) in synthesized M-TiO_2 may play an important role in enhancing the photoactivity of heterophase conjunctions. Oxygen

vacancy can act as electron donor to improve the electron transfer in the heterostructured photocatalysts.

The photo-response ability of the of pristine P-TiO_2, M-TiO_2 and CQD@TiO_2 samples was measured by using UV-Vis spectrum. For the calculation of the band gap (Eg) values two different methods can be used: the method based on Tauc graphs (conversion of spectra into Kubelka Munk absorbance units) and the first order derivative method, applied to UV-VIS spectra, recorded in reflectance mode.

Tauc plots are obtained by representing the function:

$$f(h\nu) = (\alpha \cdot h\nu)^{1/n}$$

where: α - absorption coefficient; h - Planck' constant; ν - the inverse of the λ wavelength, and n - the coefficient corresponding to the transition mode (direct transition allowed n = 1/2; indirect transition allowed n = 2)

$$h\nu = \frac{1240}{\lambda}$$

The Kubelka-Munk transformation is applied by converting the reflectance into an absorption coefficient, according to the equation:

$$\alpha = (1-R)^2 / 2R$$

From the linear extrapolation of the Tauc graphs, followed by the determination of the intersection points with the abscissa, the energy values of the band gap (Eg) are obtained [46].

It is well known that in the case of rutile, both direct (n =1/2) and indirect (n = 2) transitions take place (Eg = 3.02 - 3.24 eV), while for anatase the electron transitions are indirect (n = 2) (Eg = 2.3 - 3.59 eV) [63] (Figure 22).

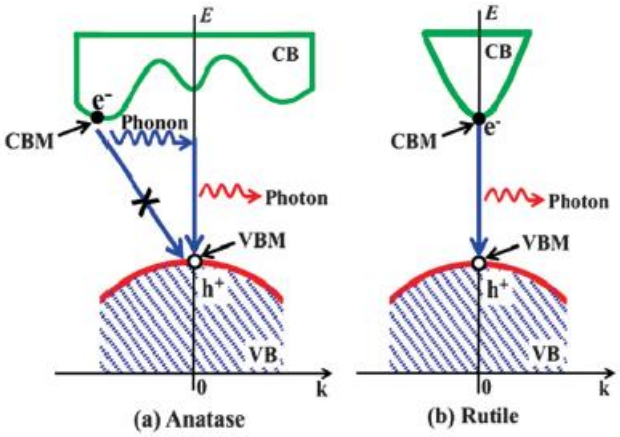

Figure 22. Comparison of recombination processes of photogenerated electrons and holes within indirect gap anatase (a) and direct gap rutile (b) (VBM - valence band maximum, CBM - conduction band minimum) [63]

The interpretation of Tauc plots becomes problematic in the case of photocatalysts consisting of several phases, such as P-TiO2 and M-TiO2. However, since TiO_2 is considered an indirect band gap semiconductor (n = 2), the E_g was estimated by the x-intercept of linear portion of Tauc's plot $((\alpha h\nu)^{1/2}$ versus hν, at $\alpha = 0$. (Figures 23 and 24).

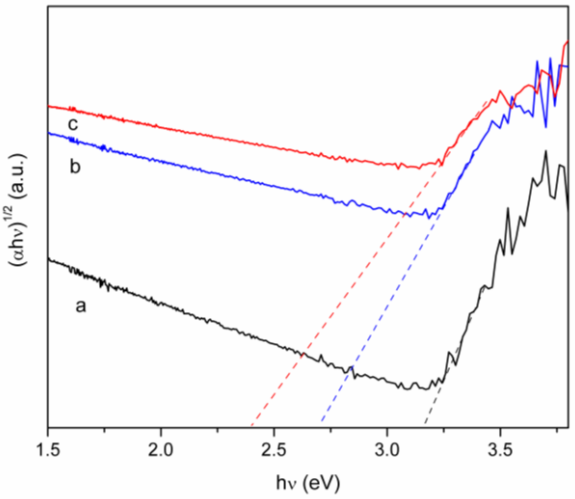

Figure 23. Plots of $(\alpha h\nu)^{1/2}$ vs. $h\nu$ for the P-TiO_2 (a), $CQD_{180\text{-}12}$@P-TiO_2 (b) and $CQD_{180\text{-}12S}$@P-TiO_2 (c) samples

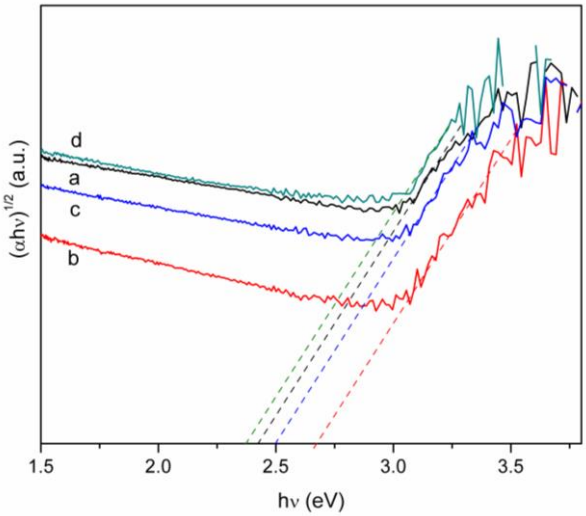

Figure 24. Plots of $(\alpha h\nu)^{1/2}$ vs. $h\nu$ for the M-TiO_2 (a), $CQD_{180\text{-}4}$@M-TiO_2 (b), $CQD_{200\text{-}4}$@M-TiO_2 (c) and $CQD_{180\text{-}12S}$@M-TiO_2 (d) samples

As Figures 23, 24 and Table 5 show that all determined band gap energies are smaller than that found for the original P-TiO_2 sample (3.15 eV).

Table 5. The E_g values obtained from Tauc plots

Sample	$E_g \pm 0.03$, eV
P-TiO_2	**3.15**
$CQD_{180\text{-}12}$@P-TiO_2	**2.70**
$CQD_{180\text{-}12S}$@P-TiO_2	**2.40**
M-TiO_2	**2.42**
$CQD_{180\text{-}4}$@M-TiO_2	**2.68**
$CQD_{200\text{-}4}$@M-TiO_2	**2.50**
$CQD_{180\text{-}12S}$@M-TiO_2	**2.38**

In the visible light range of 400 to 800 nm, anatase TiO_2 with a band gap of 3.2 eV shows no absorption, but the P-TiO_2 is a mixture of anatase TiO_2 which accounts for 84.5% and the rutile TiO_2 which accounts for 15.5% (according to the XRD analysis), thus the absorption edge expands from 387 nm to about 394 nm, with a band gap of 3.15 eV.

The M-TiO_2 sample shows a strong adsorption in the UV region with the adsorption edge at about 447 nm. Due to the high surface area and the formation of oxygen–deficient structure, bandgap energy of heterophase junction highly decreases from 3.15 (Figure 23) to 2.42 eV (Figure 24).

The band gaps of Titania materials also varied due to the CQDs presence. Therefore, in the series of P-TiO_2 based samples, the band gap decreases from 3.15 eV (P-TiO_2) to 2.70 eV ($CQD_{180\text{-}12}$@P-TiO_2) to 2.40 eV ($CQD_{180\text{-}12S}$@P-TiO_2), respectively (Figure 23, Table 5). Interesting enough, in the case of M-TiO_2 based samples, a comparison of the band gaps sizes clearly shows that except the $CQD_{180\text{-}12S}$@M-TiO_2 sample, which possess a lower band gap (2.38 eV), the $CQD_{180\text{-}4}$@M-TiO_2 and $CQD_{200\text{-}4}$@M-TiO_2 samples possess higher band gaps, i.e., 2.68 eV and 2.50 eV, respectively (Figure 25, Table 5). However, the differences are low. A schematically representation of these variations together with the % Carbon determined from elemental analysis is given in Figure 25.

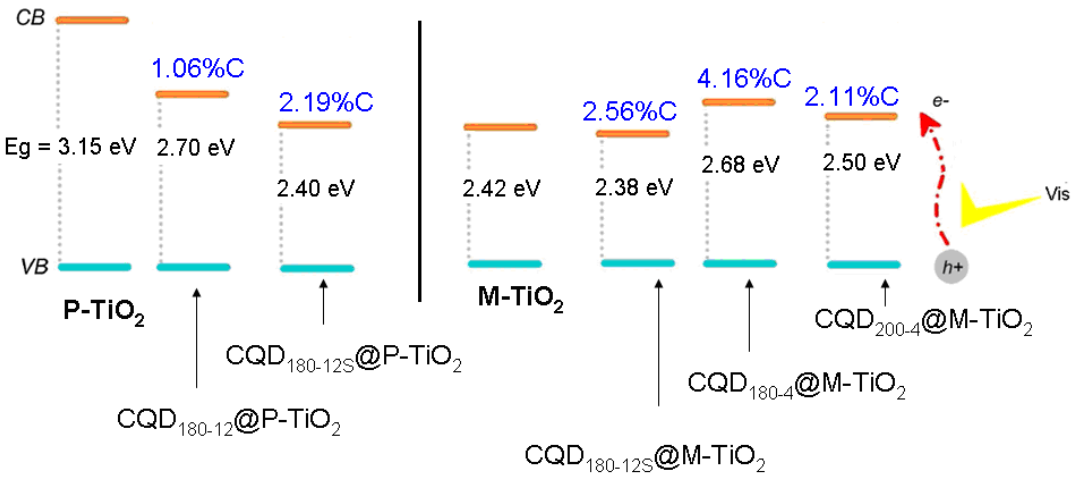

Figure 25. Schematic band diagram of the synthesized CQD@TiO2 nanocomposites. Values in blue represent the % Carbon measured in elemental analysis.

In the case of the P-TiO_2 based samples there is a direct correlation between the CQDs content and the corresponding band gap size (Figure 25). Therefore, as the CQD content increased, the corresponding band gap decreased, which is expected to generate more photoelectron–hole pairs in the visible light region.

However, for M-TiO_2 based samples, there are only slightly modifications in the band gap size of the pristine M-TiO_2 and CQDs-based nanocomposites. For the moment we have any explanation for the increased E_g of $CQD_{180\text{-}4}$@M-TiO_2 sample.

4. Catalytic tests

Figure 26 shows the chemical structure of methylene blue and the photocatalytic reaction pathway. N-dealkylation of dyes containing auxochromic alkylamine groups plays an important role in photocatalytic degradation. The color of methylene blue solutions becomes weaker when part of the methyl groups degrade, and hypochromic shift occurs. Hence, N-demethylation ($N(CH_3)_2$, 666 nm) of MB occurs as described in the pathway at first, and finally phenothiazine ring (292 nm) degredated into H_2O, CO_2, and other inorganic molecules [64].

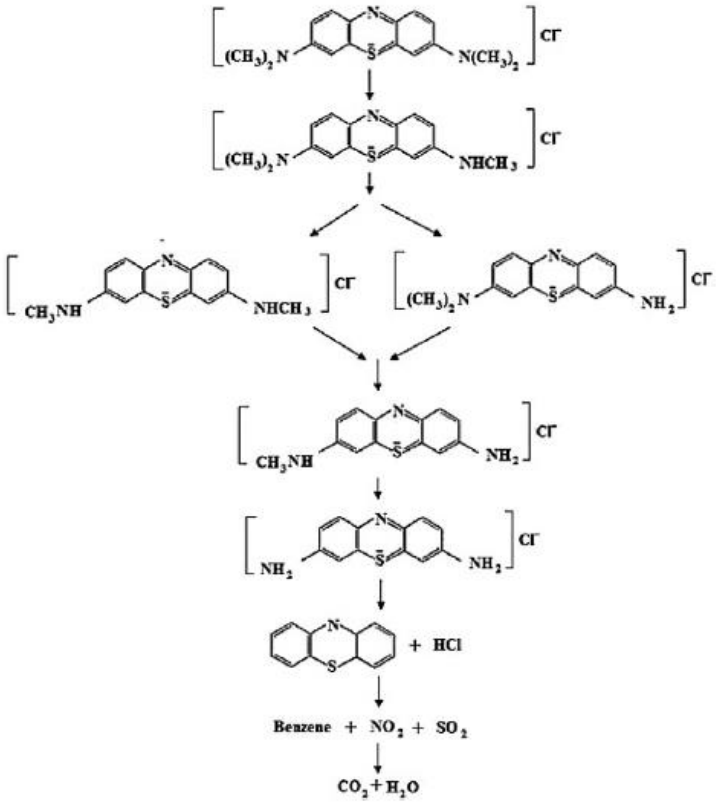

Figure 26. Chemical structure of MB and the photocatalytic reaction pathway [64]

For preliminary tests in the MB adsorption and photocatalytic degradation we have chosen two synthesized CQD-based materials with similar Carbon content and close E_g but different titania phase (P-TiO_2 and M-TiO_2), i.e. $CQD_{180\text{-}12S}$@P-TiO_2 and $CQD_{200\text{-}4}$@M-TiO_2. Obtained UV-vis spectra are shown in Figures 27-28.

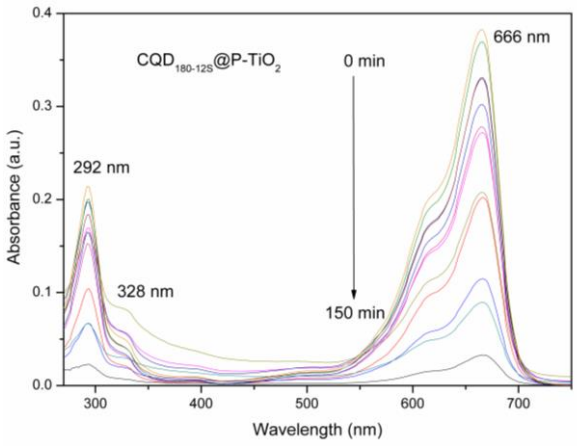

Figure 27. UV–Vis spectra of MB degradation versus reaction time in the presence of $CQD_{180\text{-}12S}$@P-TiO_2 (7.5 mg cat)

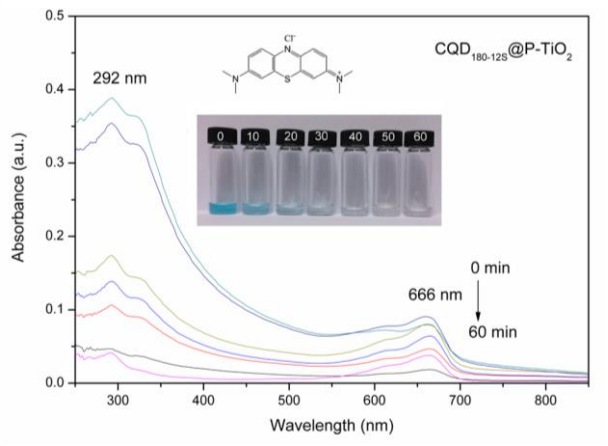

Figure 28. UV–Vis spectra of MB degradation versus reaction time in the presence of $CQD_{180\text{-}12S}$@P-TiO_2 (15 mg cat)

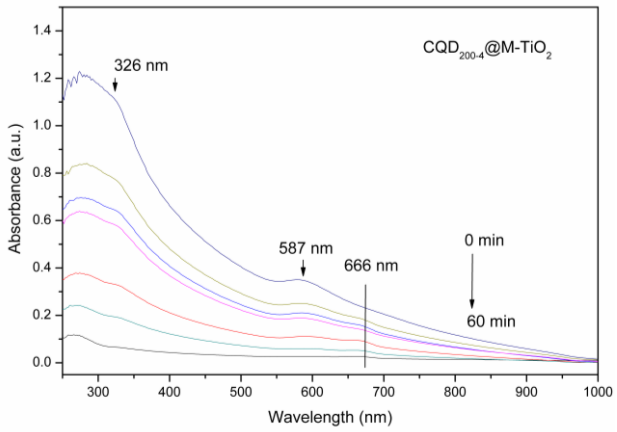

Figure 29. UV–Vis spectra of MB degradation versus reaction time in the presence of $CQD_{200\text{-}4}$@M-TiO_2 (15 mg cat)

As UV-vis spectra shows, the dimethylated groups (666 nm) are faster decomposed by comparing with phenothiazine ring (292 nm). Moreover, in the presence of the $CQD_{200\text{-}4}$@M-TiO_2 sample a new absorption peak appeared at 587 nm, which highly decreases in time.

The adsorption capacity of the P-TiO2 sample is low but the presence of the CQDs highly improved it. Therefore, in the presence of the $CQD_{180\text{-}12S}$@P-TiO_2 sample the MB adsorption was 60.7%, which increased to 74.95% on doubled amount of catalyst (Figure 30). In the presence of the $CQD_{200\text{-}4}$@M-TiO_2 (15 mg) the MB adsorption value was 90.65%.

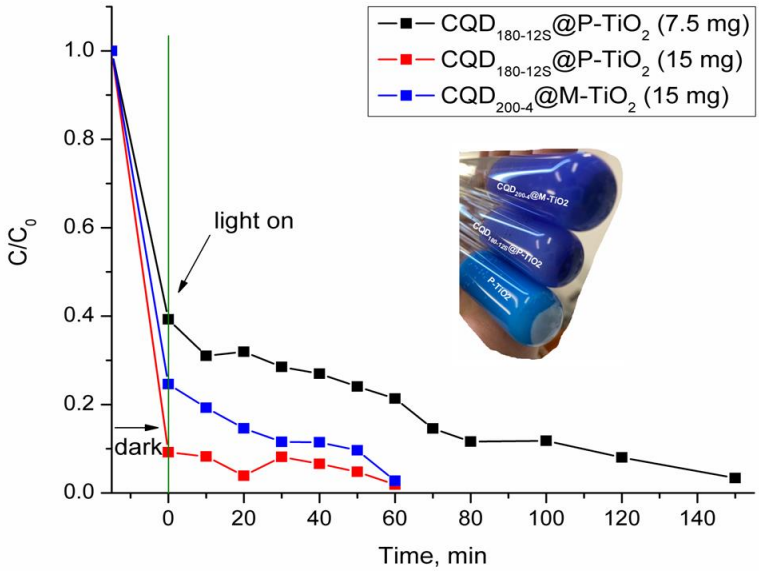

Figure 30. UV–Vis spectra of MB degradation (666 nm band) versus reaction time

High adsorption capacity of the samples can be associated with the presence of the acidic groups on the CQDs surface, making it easier to chemisorb the basic groups of MB.

Furthermore, the absorbance of MB at 666 nm [C_{Ar} = $N(CH_3)_2$] and 292 nm (phenothiazine ring) change as the reaction progress, indicating a gradually degradation of MB, in agree with [65]. However, the level of the two entities degradation is slightly different, as a function of the reaction condition (i.e., catalyst amount, reaction time) as Table 6 shows.

Table 6. The decomposition level of the $N(CH_3)_2$ and phenothiazine ring moieties as a function of the catalyst nature, catalyst amount and illumination time

Catalyst	$N(CH_3)_2$ decomposition, %	Phenothiazine ring decomposition, %
$CQD_{180\text{-}12S}$@P-TiO_2 (7.5 mg, 150 min)	96.7	97.0
$CQD_{180\text{-}12S}$@P-TiO_2 (15 mg, 60 min)	97.3	93.4
$CQD_{200\text{-}4}$@M-TiO_2 (15 mg, 60 min)	98.1	95.3

Clearly enough the photocatalytic conditions should be improved for a total mineralization of MB, more reaction conditions being necessary to be check. For the moment, we can only admit the high adsorption capacity of the generated CQD@TiO2 heterostructures and the discoloration of MB.

In agree with literature [65] a possible mechanism for the photocatalytic degradation of MB in the CQD@TiO2 system can be illustrated as in Scheme 4, which includes the following three features: i) the CQDs act as a photosensitizer to enlarge the absorption range of TiO2 into the visible light region through electronic coupling between π states of CQDs and conduction band (CB) states of TiO_2, leading to transfer of excited electrons from CQDs to the CB of TiO_2; ii) the electrons in the CB of TiO_2 react with O_2 to form $\cdot O_2^-$ and H_2O/OH is oxidized by holes at the surface of TiO_2 to produce ·OH radicals. Meanwhile, the CQDs act as an electron reservoir to trap photogenerated electrons from TiO_2 and promote separation of photogenerated electron–hole pairs; iii) the ·OH radicals react with MB and degrade it to phenothiazine rings by demethylation. The phenothiazine rings are broken down to aniline, phenol, and other intermediate aromatic ring species, which are further degraded into H2O, CO2, NH_4^+, HCOO-, and SO_4^{2+} as the final products.

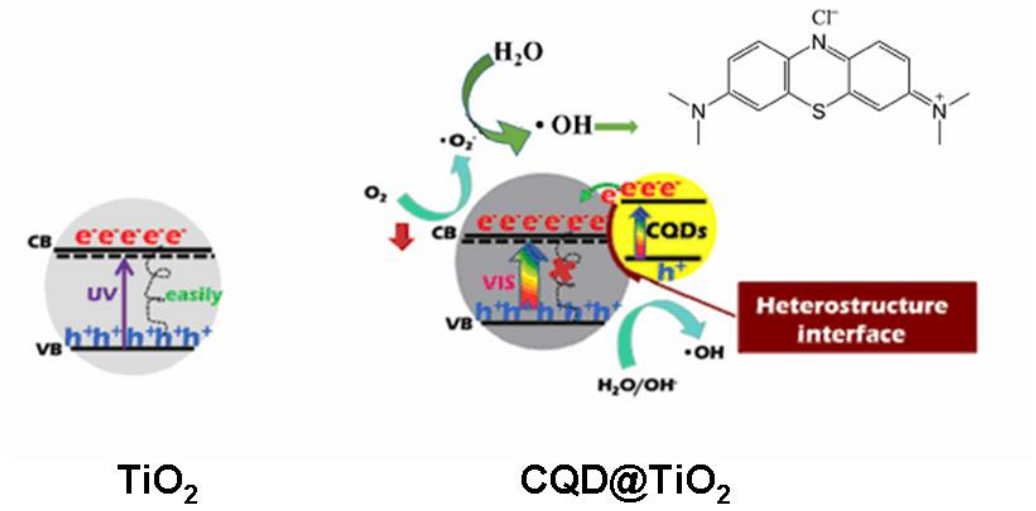

Scheme 4. Proposed mechanism in the CQDs/TiO2 heterostructure nanocomposites by adapted illustration from [65].

5. Conclusions

A facile method for the preparation of photo-luminescent CQDs based on a hydrothermal carbonization process is presented in this work using humins as the carbon precursor. The method has the advantage of being considerably cheaper than conventional methods and absolutely ‘‘green’’.

The as-prepared CQDs possess different structures and size of the carbon core, but also different composition in the shell, as a function of the hydrothermal synthesis parameters. The best CQDs in view of their size, PL properties and QY were obtained at 180C and 12h ($CQD_{180\text{-}12}$) or at 200C and 4h ($CQD_{200\text{-}4}$). Also important, the produced CQDs were readily soluble in water to form a stable, yellowish, and transparent aqueous solution without precipitation for months.

When coupling CQDs with TiO_2, the CQDs anchored on the surface of TiO_2 increases its surface roughness, resulting in the formation of a heterointerface between CQDs and TiO_2 carrier. The CQDs play an important role in the visible light photocatalytic process, as preliminary results obtained in the methylene blue degradation shows. First of all, the electrons photogenerated from the TiO_2 can be trapped by the CQDs and retard the recombination of photoexcited electron-hole pairs. What’s more, these heterostructure formed between the CQDs and the TiO_2 can greatly prolong the life of the photoexcited electron and hole pairs.

So, this work is of great interest to introduce a new and high efficiency way to fabricate visible-light heterophases photocatalysts by using cheap inorganic oxide materials and useless humins waste generated in saccharides dehydration.

Acknowledgements

This work was financially supported by The Education, Scholarship, Apprenticeships and Youth Entrepreneurship Programmer—EEA Grants 2014-2021, Project No. 18-Cop-0041.

Authors are grateful to Prof. Joanna Gościańska from Department of Chemical Technology, Faculty of Chemistry, Adam Mickiewicz University, in Poznań, Poland for performing TEM and STEM measurements.

DISEMMINATION

Experimental data obtained in this work are the subject of an abstract with the title "From humins wastes to carbon quantum dots (CQDs) based photocatalytic nanocomposites", authors: Nicolae Cristian Guzo, Magdi El Fergani, Bogdan Cojocaru, Joanna Gościańska, Vasile I. Parvulescu, Simona M. Coman, submitted to the International Workshop "Contemporary solutions for advanced materials with high impact on society (CoSoIMat)", 11-15 October 2021, Bucharest, Romania

References

[1] Coman, S. M., Tudorache, M., Parvulescu, V. I., Chapter 4: Green catalysis methods - Catalysis for lignocellulosic biomass capitalization into chemicals, In: „An introduction to green chemistry methods', R. Luque, J. C. Colmenares (Eds.), Future Science Ltd, London, UK, 2013, pp. 54-68.

[2] Sudarsanam, P., Zhong, R., Van den Bosch, S., Coman, S. M., Parvulescu, V. I., Sels B. F., Functionalised heterogeneous catalysts for sustainable biomass valorisation. Chem. Soc. Rev., 47, (2018), 8349:8e402.

[3] Saratale, G. D., Oh, S. E., Lignocellulosics to ethanol: The future of the chemical and energy industry. Afr. J. Of Biotechnol., 11, (2012), 1002:1013.

[4] Rinaldi, R., Jastrzebski, R., Clough, M. T., Ralph, J., Kennema, M., Bruijnincx P. C. A., Weckhuysen. B. M., Paving the way for lignin valorisation: recent advances in bioengineering, biorefining and catalysis. Angew. Chem., Int. Ed., 55, (2016), 8164:8215.

[5] Clark, J., Deswarte, F., Introduction to chemicals for biomass. Second edition, John Wiley & Sons Ltd., 2015, Chapter 1. The biorefinery concept: An integrated approach, pgs. 1-31.

[6] Serrano-Ruiz, J. C., Luque, R., Sepúlveda-Escribano, A., Transformations of biomass-derived platform molecules: from high added-value chemicals to fuels via aqueous-phase processing. Soc. Rev., 40, (2011), 5266:5281.

[7] Mija, A., van der Waal, J. C., Pin, J.-M., Guigo, N., de Jong, E., Humins as promising materials for producing sustainable carbohydrate-derived building materials. Construction and Building Materials, 139, (2017), 594:601.

[8] Sevilla, M.; Fuertes, A.B., The production of carbon materials by hydrothermal carbonization of cellulose Carbon, 47, (2009), 2281:2289.

[9] Mija, A., van der Waal, J. C., Pin, J.-M., Guigo, N., de Jong, E., Humins as promising material for producing sustainable polyssacharide-derived building materials., Proceedings of the First International Conference on Bio-based Building Materials, 22-24/06/2015 Clermont-Ferrand, France, 1:6.

[10] van Zandvoort, I., Wang, Y., Rasrendra C.B., van Eck, E.R.H., Bruijnincx, P.C.A., Heeres, H.J., Weckhuysen., B.M., Formation, Molecular Structure, and Morphology of Humins in Biomass Conversion: Influence of Feedstock and Processing Conditions. ChemSusChem, 6, (2013), 1745:1758.

[11] Hoang, T.M.C., Lefferts, L., Seshan, K., Valorization of Humin-Based Byproducts from Biomass Processing – A Route to Sustainable Hydrogen. ChemSusChem, 6, (2013), 1651:1658.

[12] Xu, X., Ray, R., Gu, Y., Ploehn, H. J., Gearheart, L., Raker, K., Scrivens, W. A., Electrophoretic Analysis and Purification of Fluorescent Single-Walled Carbon Nanotube Fragments. J. Am. Chem. Soc., 126, (2004), 12736:12737.

[13] Sun, Y.-P., Zhou, B., Lin, Y., Wang, W., Fernando, K. S., Pathak, P., Meziani, M. J., Harruff, B. A., Wang, X., Wang, H., Quantum-sized carbon dots for bright and colorful photoluminescence. J. Am. Chem. Soc., 128, (2006), 7756:7757.

[14] Baker, S. N., Baker, G. A., Luminescent Carbon Nanodots: Emergent Nanolights. Angew. Chem., Int. Ed., 49, (2010), 6726:6744.

[15] Wang, Y., Hu, A., Carbon quantum dots: synthesis, properties and applications. J. Mater. Chem. C, 2, (2014), 6921:6939.

[16] Wang, R., Lu, K.-Q., Tang, Z.-R., Xu, Y.-J., Recent progress in carbon quantum dots: synthesis, properties and applications in photocatalysis. J. Mater. Chem. A, 5, (2017), 3717:3734.

[17] Li, H. T., Liu, R. H., Lian, S. Y., Liu, Y., Huang, H., Kang, Z.H., Near-infrared light controlled photocatalytic activity of carbon quantum dots for highly selective oxidation reaction Nanoscale, 5, (2013), 3239:3257.

[18] Liu, J., Zhu, W., Yu, S., Yan, X., Three dimensional carbogenic dots/TiO_2 nanohetero-junctions with enhanced visible light-driven photocatalytic activity. Carbon, 79, (2014) 369:379.

[19] Ohno, T., Sarukawa, K., Tokieda, K., Matsumura, M., Morphology of a TiO_2 Photocatalyst (Degussa, P-25) Consisting of Anatase and Rutile Crystalline Phases. J Catal., 203, (2001), 82:86.

[20] Hoffmann, M.R., Martin, S.T., Choi, W., Bahnemann, D.W., Environmental Applications of Semiconductor Photocatalysis. Chem. Rev. 95, (1995), 69:96.

[21] Alvaro, M., Aprile, C., Benitez, M., Carbonell, E., Garcia, H., Photocatalytic Activity of Structured Mesoporous TiO_2 Materials.J. Phys. Chem. B 110, (2006), 6661:6665.

[22] Tian, G.H., Fu, H.G., Jing, L.Q., Xin, B.F., Pan, K., Preparation and Characterization of Stable Biphase TiO_2 Photocatalyst with High Crystallinity, Large Surface Area, Enhanced Photoactivity. J. Phys. Chem. C 112, (2008), 3083:3089.

[23] Kang, C.H., Jing, L.Q., Guo, T., Cui, H.C., Zhou, J., Fu, H.G., Mesoporous SiO_2-Modified Nanocrystalline TiO_2 with High Anatase Thermal Stability and Large Surface Area as Efficient Photocatalyst. J. Phys. Chem. C 113, (2009), 1006:1013.

[24] Janus, M., Morawski, A.W., New method of improving photocatalytic activity of commercial Degussa P25 for azo dyes decomposition. Appl. Catal. B 75, (2007), 118:123.

[25] Yu, J.C., Lin, J., Lo, D., Lam, S.K., Influence of Thermal Treatment on the Adsorption of Oxygen and Photocatalytic Activity of TiO_2. Langmuir 16, (2000), 7304:7308.

[26] Murgolo, S., Petronella, F., Ciannarella, R., Comparelli, R., Agostiano, A., Curri, M.L., Mascolo, G., UV and solar-based photocatalytic degradation of organic pollutants by nano-sized TiO_2 grown on carbon nanotubes. Catal. Today, 240, (2015), 114:124.

[27] Zhang, Z. P., Zhang, J., Chen, N., Qu, L. T., Graphenequantum dots: an emerging material for energy-related applications and beyond. Energy and Environ. Sci., 5, (2012), 8869:8890.

[28] Wang, X., Cao, L., Lu, F. S., Meziani, M. J., Li, H. T., Qi, G., Zhou, B., Harruff, B. A., Kermarrec, F., Sun, Y. P., Photoinduced electron transfers with carbon dots. Chem. Commun., 2009, 3774:3776.

[29] Yao, Y., Li, G. H., Ciston, S., Lueptow, R. M., Gray, K. A., Photoreactive TiO2/carbon nanotube composites: synthesis and reactivity. Environ. Sci. Technol., 42, (2008), 4952:4957.

[30] El Fergani, M., Candu, N., Tudorache, M., Bucur, C., Djelal, N., Granger, P., Coman, S. M., From useless humins by-product to Nb@ graphite-like carbon catalysts highly efficient in HMF synthesis. Appl. Catal. A: General, 618, (2021) 118:130.

[31] Prasannan, A. Imae, T., One-Pot Synthesis of Fluorescent Carbon Dots from Orange Waste Peels. Ind. Eng. Chem. Res., 52, (2013), 15673:15678.

[32] Yu, H., Zhao, Y., Zhou, C., Shang, L., Peng, Y., Cao, Y., Wu, L.-Z., Tunga, C.-H., Zhang, T., Carbon quantum dots/TiO_2 composites for efficient photocatalytic hydrogen evolution. J. Mater. Chem. A, 2, (2014), 3344:3351.

[33] Galanin, M. D., Kut'enkov, A. A., Smorchkov, V. N., Timofeev, Y. P., Chizhikov, Z. A., Opt. Spektrosk. 53, (1982), 683:690.

[34] Chen X., Zhang W., Wang Q., Fan J., C_8-structured carbon quantum dots: Synthesis, blue and green double luminescence, and origins of surface defects. Carbon, 79, (2014), 165:173.

[35] Peng, H., Sejdic, J. T., Simple Aqueous Solution Route to Luminescent Carbogenic Dots from Carbohydrates. Chem. Mater., 21, (2009), 5563:5565.

[36] Loh, K.P., Bao, Q., Eda, G., Chhowalla, M., Graphene oxide as a chemically tunable platform for optical applications. Nat. Chem. 2, (2010), 1015:1024.

[37] Wang, C., Xu, Z., Cheng, H., Lin, H., Humphrey, M. G., Zhang, C., A hydrothermal route to water-stable luminescent carbon dots as nanosensors for pH and temperature. Carbon, 82, (2015), 87:95.

[38] Peng, W., Xueyun, W., Wei, L., Yushan, L., Zhijun, C., Shouxin, L., Ultra-small amorphous carbon dots: preparation, photoluminescence properties, and their application as TiO2 photosensitizers. J. Mater. Sci., 54, (2019), 5280:5293.

[39] H. Liu, X. Zhao, F. Wang, Y. Wang, L. Guo, J. Mei, C. Tian, X. Yang, D. Zhao, High-Efficient Excitation-Independent Blue Luminescent Carbon Dots. Nanoscale Research Letters 12, (2017), 1:7.

[40] Song, Y., Zhu, S., Xiang, S., Zhao, X., Zhang, J., Zhang, H., Fu, Y., Yang, B., Investigation into the fluorescence quenching behaviors and applications of carbon dots. Nanoscale, 6, (2014), 4676:4682.

[41] Khan, S., Gupta, A., Verma, N., Nandi, C., Time-Resolved Emission Reveals Ensemble of Emissive States as the Origin of Multicolor Fluorescence in Carbon Dots. Nano Lett, 15, (2015), 8300:8305.

[42] Han, L., Liu, S.G., Dong, J.X., Liang, J.Y., Li, L.J., Li, N.B., Luo, H.Q., Facile synthesis of multicolor photoluminescent polymer carbon dots with surface-state energy gap-controlled emission. J. Mater. Chem. 5, (2017), 10785:10793.

[43] Zhu, S, Song, Y, Wang, J, Wan, H, Zhang, Y, Ning, Y, Yang, B., Photoluminescence in graphene quantum dots. Nano Today, 13, (2017), 10:14.

[44] Li, H., He, X., Liu, Y., Yu, H., Kang, Z., & Lee, S-T., Synthesis of fluorescent carbon nanoparticles directly from active carbon via a one-step ultrasonic treatment. Materials Research Bulletin, 46, (2011), 147:151.

[45] X. Wen, P. Yu, Y.-R. Toh, X. Ma, J. Tang, On the upconversion fluorescence in carbon nanodots and graphene quantum dots. Chem. Commun., 50, (2014), 4703:4706.

[46] Zhang, Y., Tang, Z.R., Fu, X., Xu, Y.J., TiO_2−Graphene Nanocomposites for Gas-Phase Photocatalytic Degradation of Volatile Aromatic Pollutant: Is TiO_2−Graphene Truly Different from Other TiO_2−Carbon Composite Materials. ACS Nano, 4, (2010), 7303:7314.

[47] Tang, H., Chang, S. F., Jiang, L. Y., Tang, G. G., Liang, W., Novel spindle-shaped nanoporous TiO_2 coupled graphitic g-C_3N_4 nanosheets with enhanced visible-light photocatalytic activity. Ceram. Int., 42, (2016) 18443:18452.

[48] Yang D., Zhao J., Liu H., Zheng Z., Adebajo M., Wang H., Liu X., Zhang H., Zhao J., Bell J., Zhu H., Enhancing photoactivity of TiO_2(B)/anatase core-shell nanofibers by selectively doping cerium ions into the TiO_2 (B) core.Chem. Eur. J., 19, (2013), 5113:5119.

[49] Zhang, Q.H., Gao, L., Guo, J.K., Effects of calcination on thephotocatalytic properties of nanosized TiO_2 powders prepared by $TiCl_4$ hydrolysis. Appl. Catal. B, 26, (2000), 207:215.
[50] Spurr, R. A., Myers, H., Quantitative Analysis of Anatase-Rutile Mixtures with an X-Ray Diffractometer. Anal Chem, 29, (1957), 760:762.
[51] Wu, P., Wu, X., Li, W., Liu, Y., Chen, Z., Liu, S., Ultra-small amorphous carbon dots: preparation, photoluminescence properties, and their application as TiO_2 photosensitizers. J. Mater. Sci. 54, (2019), 5280:5293.
[52] He, J., Du, Y.-en, Bai, Y., An, J., Cai, X., Chen, Y., Wang, P., Yang, X., Feng, Q., Facile Formation of Anatase/Rutile TiO_2 Nanocomposites with Enhanced Photocatalytic Activity. Molecules 24, (2019), 2996:3010.
[53] Tsai, C. C., Teng, H., Regulation of the Physical Characteristics of Titania Nanotube Aggregates Synthesized from Hydrothermal Treatment. Chem. Mater. 16, (2004), 4352:4358.
[54] Chen, Q., Zhou, W. Z., Du, G. H., Peng, L. M., Trititanate Nanotubes Made via a Single Alkali Treatment. Adv. Mater. 14, (2002), 1208:1211.
[55] Du, G. H., Chen, Q., Che, R. C., Yuan, Z. Y., Peng, L. M. Preparation and structure analysis of titanium oxide nanotubes. Appl. Phys. Lett., 22, (2001), 3702:3704.
[56] Dong-Seok, S., Jong Kook, L., Hwang, K., Preparation of nanotube-shaped powder TiO_2. J. Crystal Growth, 229, (2001), 428:432.
[57] Lazzeri, M., Vittadini, A., Selloni, A., Structure and energetics of stoichiometric TiO2 anatase surfaces. Phys. Rev. B, 63, (2001), 155409:155421.
[58] Liu, R., Duan, L., Shen, H., Zhang, Y., Zhao, X., In situ synthesis and enhanced visible light photocatalytic activity of C-TiO2microspheres/carbon quantum dots. Ceram. Int., 43, (2017), 8648:8654.
[59] Hassan, M.E., Cong, L., Liu, G., Zhu, D., Cai, J., Synthesis and characterization of C-doped TiO2 thin films for visible-light-induced photocatalytic degradation of methyl orange. Appl. Surf. Sci., 294, (2014), 89:94.
[60] Miao, R., Luo, Z., Zhong, W., Chen, S.-Y., Jiang, T., Dutta, B., Nasr, Y., Zhang, Y., Suib, S.L., Mesoporous TiO2 modified with carbon quantum dots as a high-performance visible light photocatalyst. Apl. Catal. B Environ., 189, (2016), 26:38.
[61] Yu, B.Y., Kwak, S.Y., Carbon quantum dots embedded with mesoporous hematite nanospheres as efficient visible light-active photocatalysts. J. Adv. Ceram., 22, (2012), 8345:8353.

[62] K.N.P. Kumar, J. Kumar, K. Keizer, Effect of peptization on densification and phase transformation behaviour of sol-gel-derived nanostructured titania. J. Am. Ceram. Soc., 77, (1994), 1396:1400.

[63] Zhang, J., Zhou, P., Liu, J., Yu, J., New understanding of the difference of photocatalytic activity among anatase, rutile and brookite TiO_2. Phys. Chem. Chem. Phys., 16, (2014), 20382:20386.

[64] Zhang, T.Y., Oyama, T., Aoshima, A., Hidaka, H., Zhao, J.C., Serpone, N., Kinetics of Photocatalytic Degradation of Methylene Blue in Aqueous Dispersions of TiO_2 Nanoparticles under UV-LED Irradiation. J. Photochem. Photobiol. A, 140, (2001), 163:172.

[65] Wu, P., Wu, X., Li, W., Liu, Y., Chen, Z., Liu, S., Ultra-robust carbon fibers for multi-media purification via solar-evaporation. J Mater Sci., 54, (2019), 5280:5293.

ADAM MICKIEWICZ UNIVERSITY IN POZNAŃ
Faculty of Chemistry

Prof. UAM Dr. Habil. Joanna Gościańska
Department of Chemical Technology
tel. (61) 829-16-07
e-mail: asiagosc@amu.edu.pl

Poznań, 19.06.2021 r.

I, undersigned Joanna Gościańska, professor at Department of Chemical Technology, Faculty of Chemistry, Adam Mickiewicz University in Poznań, Poland, declare that I agree that the student Nicolae-Cristian Guzo can use the data obtained from the TEM and STEM measurements on CQD@TiO_2 samples, in the dissertation thesis that he will defend in the July 2021 session, at the Faculty of Chemistry, University of Bucharest.

These measurements were performed in the laboratories of the above-mentioned faculty, in a frame of a scientific collaboration between me and Prof. Simona Coman, regarding the synthesis and characterization of photocatalytic nanocomposites, in which the student Nicolae-Cristian Guzo was also involved.

Joanna Gościańska